Journal of Materials Science & Technology 75 (2021) 225–251

Contents lists available at ScienceDirect

Journal of Materials Science & Technology

journal homepage: www.jmst.org

Invited Review

Polymer matrix wave-transparent composites: A review

Lin Tang [a], Junliang Zhang [a,c,*], Yusheng Tang [a], Jie Kong [a], Tianxi Liu [b], Junwei Gu [a,*]

[a] Shaanxi Key Laboratory of Macromolecular Science and Technology, School of Chemistry and Chemical Engineering, Northwestern Polytechnical University, Xi' an 710072, China
[b] State Key Laboratory for Modification of Chemical Fibers and Polymer Materials, Donghua University, Shanghai 201620, China
[c] School of Materials Science and Engineering, Henan University of Science and Technology, Luoyang 471023, China

ARTICLE INFO

Article history:
Received 12 August 2020
Received in revised form
10 September 2020
Accepted 19 September 2020
Available online 21 October 2020

Keywords:
Polymer matrix wave-transparent composites
Reinforced fibers
Surface functionalization
Testing methods
Application prospect

ABSTRACT

With the rapid development of electronic information technology, antenna systems in the fields of aviation, aerospace, transportation, and 5 G communication services are becoming more and more intensive and accurate. Polymer matrix wave-transparent composites with lightweight, low dielectric constant (ϵ) and dielectric loss tangent ($\tan\delta$), high temperature resistance, and excellent mechanical properties are urgently needed in order to ensure high-fidelity transmission of electromagnetic wave and protect antenna systems from external interference. This review introduces the wave transmission mechanism, key compositions (polymer matrix & reinforced fibers), and several typical testing methods for dielectric properties of polymer matrix wave-transparent composites, mainly elaborates the latest research progress and achievements of polymer matrix wave-transparent composites from polymer matrix, reinforced fibers and their surface functionalization methods, and presents the key scientific and technical problems that need to be solved urgently in the application of polymer matrix wave-transparent composites in the antenna systems. Finally, the future development trends and application prospects of the polymer matrix wave-transparent composites are also proposed.

Contents

* Corresponding authors at: Shaanxi Key Laboratory of Macromolecular Science and Technology, School of Chemistry and Chemical Engineering, Northwestern Polytechnical University, Xi' an 710072, China.
E-mail addresses: junliang.zhang@nwpu.edu.cn (J. Zhang), gjw@nwpu.edu.cn, nwpugjw@163.com (J. Gu).

https://doi.org/10.1016/j.jmst.2020.09.017
1005-0302/

1. Introduction

Wave-transparent composites refer to the functional composites that can transmit electromagnetic wave at a certain frequency, and have been widely used in the fields of missiles, launch vehicles, aircrafts, microwave towers, microwave relay stations, radomes and antenna window of communication antennas, and high-performance printed circuit boards (PCB) [1–5]. In addition, wave-transparent composites can protect radar antennas, communication and microwave systems from harsh external environment, and provide electromagnetic windows for transmission and reception of antenna electromagnetic wave, to ensure their long-term efficient operation [6–8].

With the rapid development of electronic information technology, the technical intensity and accuracy of antenna systems [9,10], as well as the frequency of electromagnetic wave emission and reception are getting higher and higher, and the 5 G signal transmission [11] is also getting faster and faster [12–14], which puts forward higher requirements for wave transmission efficiency, load bearing, heat insulation, impact resistance, weather resistance, and air tightness of the wave-transparent composites [15]. Polymer matrix wave-transparent composites (Fig. 1) have shown broad application prospects in the fields of aviation/aerospace, transportation, and 5 G communication services due to their advantages of lightweight, high strength, low dielectric constant (ϵ) and dielectric loss tangent value ($\tan\delta$), strong designability, good structural stability, and material/structure/function integration, and so on [16–18].

This review introduces the wave transmission mechanism, key compositions (polymer matrix & reinforced fibers), and the several typical testing methods for dielectric properties of polymer matrix wave-transparent composites, mainly elaborates the latest research progress and achievements of polymer matrix wave-transparent composites from polymer matrix, reinforced fibers, and their surface functionalization methods, and also presents the key scientific and technical problems that need to be solved urgently in the application of polymer matrix wave-transparent composites in the antenna system. Finally, the future development trends and application prospects of polymer matrix wave-transparent composites are also proposed.

2. Definition of polymer matrix wave-transparent composites

Polymer matrix wave-transparent composites refer to lightweight & advanced composites with both load bearing capacity and wave transmission performance, which are mainly composed of reinforced fibers and polymer matrix, and fabricated by the methods of hot pressing, vacuum bag or resin transfer molding [19,20]. The comprehensive properties of the polymer matrix wave-transparent composites mainly depend on the polymer matrix phase, the reinforced fibers phase, and the interface (Fig. 2) of the reinforced fibers/polymer matrix [21,22].

Polymer matrix mainly plays the role of bonding and partially bearing in the composites, and its heat resistance determines the final thermal stability of the composites [23]. However, the dielectric properties of different polymer matrix vary greatly. Therefore, choosing a suitable polymer matrix is beneficial to fabricating polymer matrix wave-transparent composites with high wave transmission efficiency. Reinforced fibers mainly play the role of reinforcement and bearing in the composites [24]. However, the ϵ value of reinforced fibers is generally larger than that of polymer matrix. Therefore, the intrinsic mechanical properties and dielectric properties of the reinforced fibers must be considered. Moreover, the interface of the reinforced fibers/polymer matrix is the link between the two phases. Excellent interfacial compatibility would make the mechanical properties and dielectric properties of the reinforced fibers fully exert [25,26].

3. Wave transmission mechanism of the polymer matrix wave-transparent composites

Wave transmission performance of the polymer matrix wave-transparent composites is usually evaluated by ϵ and $\tan\delta$ [27,28]. The ϵ can characterize the dielectric or polarization of the composites, which is the capacitance ratio of the same size capacitor with dielectrics under vacuum [29–31]. And ϵ can also characterize the storage capacity of the composites. Dielectric loss means that part electromagnetic wave is consumed when transmitting through the medium, which is then converted into heat energy. Dielectric loss is generally expressed as $\tan\delta$ [32]. Moreover, the

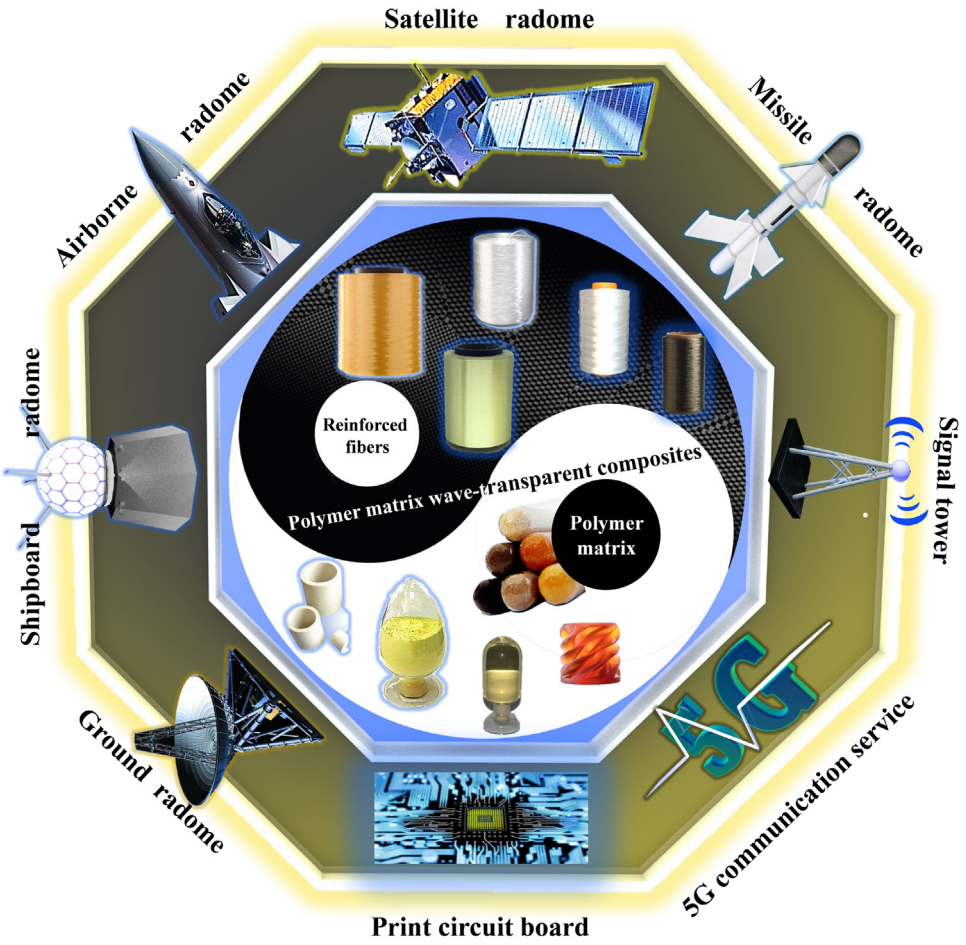

Fig. 1. Brief introduction of the polymer matrix wave-transparent composites and their typical applications.

relationship between the total loss value (α) of the electromagnetic wave transmitted in the medium, ϵ, tanδ, and electromagnetic wave frequency (f) is shown in Eq. (1).

$$\alpha = \epsilon^{1/2} f \cdot tan\delta \tag{1}$$

The α is proportional to ϵ and tanδ. As ϵ and tanδ decrease, the electromagnetic wave loss during transmission also reduces [33]. According to the law of energy conservation, when transmitting through the medium [34], electromagnetic wave is divided into transmitted wave, reflected wave, and loss (Fig. 3). Electromagnetic wave reflection mainly occurs at the interface between the medium and air. According to the impedance matching theory [35], the larger the ϵ of the medium, the more electromagnetic wave is reflected, thereby reducing the electromagnetic wave transmission efficiency [36,37]. The electromagnetic wave loss is mainly due to the polarization phenomenon of the medium in the external electric field, which causes the electromagnetic wave energy loss [38] (polarization phenomenon, such as electronic polarization or atomic polarization, is a kind of resonance or elastic process, in which energy dissipation occurs).

What's more, when the electromagnetic wave is incident on the medium, the relationship of reflection coefficient (Γ), energy loss (A), and wave transmission coefficient (T) is as follows [39]:

$$A = \frac{2\pi d\epsilon \tan\delta}{\lambda(\delta - \sin^2\theta)^{1/2}} \tag{2}$$

$$\Gamma = \frac{(\epsilon - \sin^2\theta)^{(1/2)} - \epsilon\cos\theta}{(\epsilon - \sin^2\theta)^{(1/2)} + \epsilon\cos\theta} \tag{3}$$

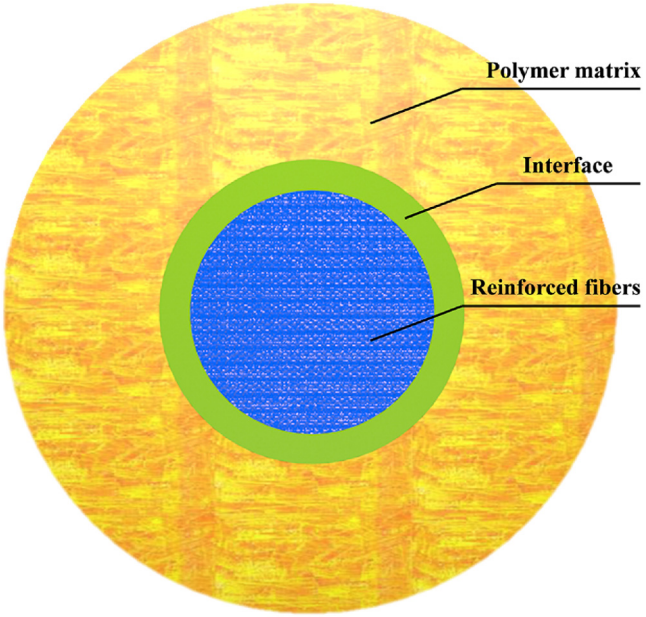

Fig. 2. Schematic diagram of key composition for polymer matrix wave-transparent composites.

$$|T|^2 = \frac{(1-\Gamma^2)^2}{(1-\Gamma^2)^2 + 4\Gamma^2\sin^2\varphi} \tag{4}$$

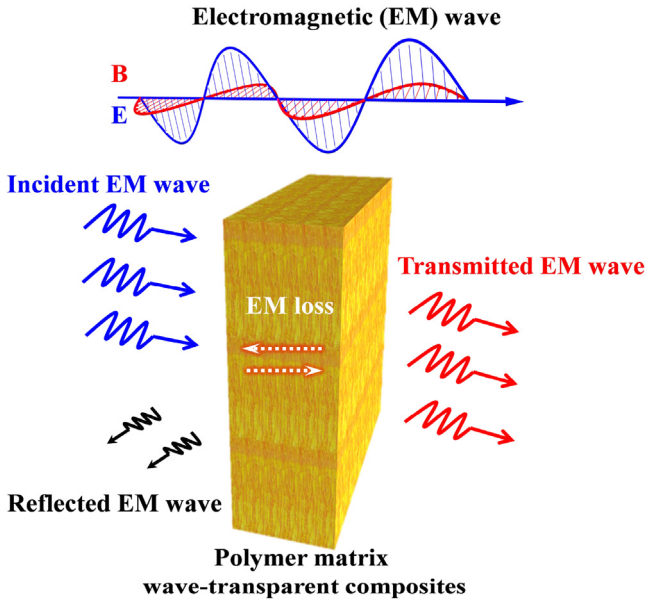

Fig. 3. Schematic diagram of electromagnetic wave transmission for polymer matrix wave-transparent composites.

where $\varphi = \frac{2\pi d}{\lambda}(\epsilon - \sin^2\theta)^{1/2}$; d represents the thickness of the composites; λ represents the wave length of the electromagnetic wave; θ represents the angle of incidence on the surface of the composites. According to Eqs. (2)–(4), the larger the ϵ and tanδ, the more electromagnetic wave is reflected and the more energy of electromagnetic wave is lost in the medium, thereby reducing the T.

In addition, polymer matrix wave-transparent composites are composed of mediums with different ϵ (reinforced fibers, ϵ_1; polymer matrix, ϵ_2). According to the Lichtenecher mixing rule [40], the theoretical ϵ of polymer matrix wave-transparent composites can be calculated from Eq. (5).

$$\log \epsilon = V_0 \log \epsilon_0 + V_1 \log \epsilon_1 + V_2 \log \epsilon_2 \tag{5}$$

where, $\epsilon_0$represents the dielectric constant of air, V_1, V_2, and V_0 represent the volume fraction of the fiber phase, polymer matrix phase, and pores in the total volume of the polymer matrix wave-transparent composites, respectively, in which $V_1 + V_2 + V_0 = 1$. However, the above equation can only roughly estimate the ϵ of the polymer matrix wave-transparent composites. Choosing reinforced fibers and polymer matrix with low ϵ and tanδ values is beneficial to obtaining polymer matrix wave-transparent composites with high T. Besides, the relationship between ϵ and the internal structure of the medium can be calculated from Debye formula (6) [41].

$$\epsilon = 1 + 3\frac{N\alpha}{3\epsilon_0 - N\alpha} \tag{6}$$

where, N represents the number of atoms in a unit volume and the density of polarized molecules; α represents the polarizability. From Eq. (6), reducing the density and polarizability of polarized molecules is beneficial to descreasing the ϵ, thereby increasing the T of polymer matrix wave-transparent composites.

According to the microscopic mechanism of dielectric polarization, the polarization types can be divided into the following five categories [42–44]:

3.1. Electronic polarization

Under the external electric field, the peripheral electron cloud in the molecules, atoms, or ions that make up the dielectric is elastically displaced relative to the nucleus to induce a dipole moment, which is called electronic polarization (Fig. 4(a)). The required time for the process of electronic polarization is extremely short, about 10^{-15}–10^{-13} s. When the external electric field is removed, the induced dipole moment is immediately restored without energy loss. Therefore, electronic polarization is also called reversible polarization or elastic polarization. Passchier et al. [45] constructed and operated a compton polarimeter to measure the longitudinal polarization of a stored electron beam. The compton polarimeter was operated normally on the internal target device where polarized electrons were generated and to measure the electronic polarization during its internal electronic operation. Jenkins et al. [46] used a non-local dielectric theory to describe the electronic polarization induced by perturbing fields, and to characterize spontaneous, quantum mechanical fluctuations in the polarization. According to the fluctuation-dissipation theorem, for a molecule in equilibrium state under a radiation bath at a fixed temperature, the fluctuating electron polarization was positively related to the dielectric function when correlating the spontaneous polarization fluctuations to the imaginary part of the non-local polarizability density.

3.2. Atomic polarization

When the molecular skeleton is deformed by external electric field, the positive and negative charge centers in the molecules will be relatively displaced. The process of atomic polarization takes about 10^{-13} s, and the molecular deformation process is accompanied by a slight energy loss (Fig. 4(b)). Li et al. [47] adopted the wave function Cornu curl and the real & imaginary parts of the wave function to investigate the process of atomic polarization, and proposed a calculation method for the atomic polarization radius. The obtained calculation results were generally better than those based on Norman rules.

3.3. Ionic polarization

Under external electric field, a relative elastic displacement occurs between the positive and negative ions, which cause an induced dipole moment. The corresponding polarization diagram of the ionic polarization is similar to that of atomic polarization. Ionic polarization generally exists inside ionic crystals composed of ionic bonds or crystalline phases of ceramic media. Similar to that of electronic polarization, the formation and disappearance time of ionic polarization is extremely short without energy loss. Wang et al. [48] analyzed the ion migration and dielectric behavior of $NaNbO_3$ at 29.1 GPa. The interaction between Na^+ and NbO_6 enhanced the vibration resonance damping of the system. In the high-pressure stage, the ionic polarization and space charge polarization of the $NaNbO_3$ interface layer affected its dielectric properties.

3.4. Orientation polarization

Orientation polarization is also known as dipolar polarization. Polar molecules with permanent dipole moments are aligned under the external electric field (Fig. 4(c)). In the natural state, the irregular thermal motion of molecules causes their distribution to be equal in each direction. The rotation of polar molecules in the direction of the external electric field needs to overcome their own inertia and rotational resistance, which requires a long time for orientation polarization, about 10^{-9} s. The orientation polarization of polymers presents different unit orientations (side chain groups and the orientation of the entire molecular chain), resulting in a longer time for orientation polarization, similar to that of mechanical relaxation. Wu et al. [49] investigated the dipole-oriented

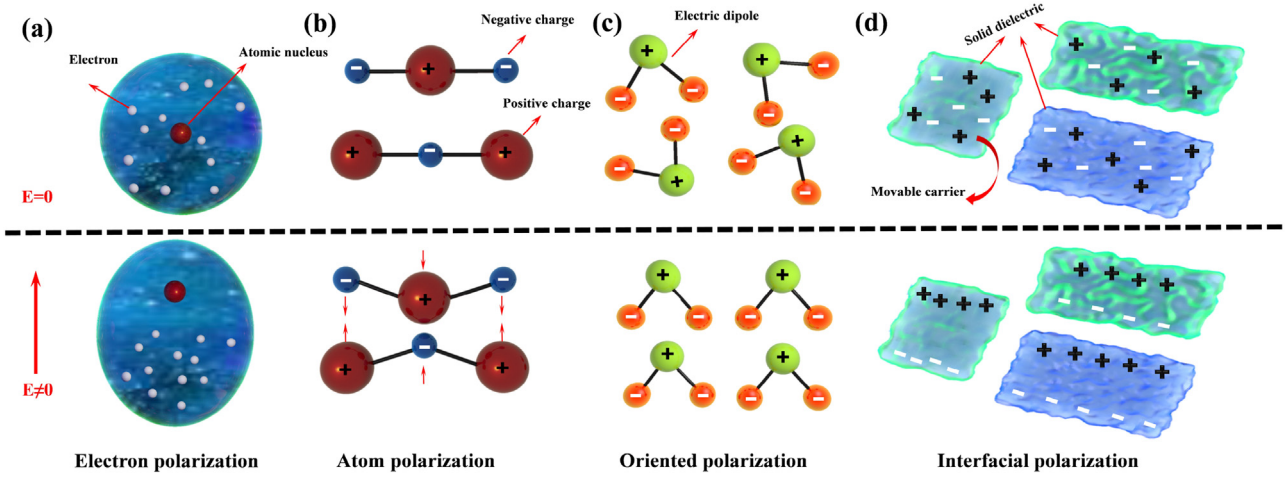

Fig. 4. Schematic diagram of dielectric polarization: electron polarization (a), atom polarization (b), orientation polarization (c), and interfacial polarization (d).

polarization characteristics of polar monolayer under external electric field by measuring the change of fluorescence polarization characteristics of the monolayer. The polar single molecules of the polymethyl methacrylate film displayed directional distribution.

3.5. Interfacial polarization

Interfacial polarization is the main form of polarization in a non-uniform phase medium. Under the external electric field, carriers accumulate at the interface between the two phases or are trapped by defects, causing charge accumulation and uneven charge distribution in the medium and resulting in electric dipole moment (Fig. 4(d)). Such polarization takes a long time, from tenths of a second to a few minutes. Ma et al. [50] investigated dielectric behavior of the polymer-derived amorphous silicon carbonitride. The interfacial polarization occurs at the interface between the silicon carbonitride phase and the free carbon phase, mainly due to the migration and accumulation of charge carriers. And the interfacial polarization of the polymer-derived amorphous silicon carbonitride was enhanced at elevated temperatures, resulting in an increase in ϵ and tanδ.

Electron polarization and orientation polarization are both called as deformation polarization or induced polarization, and the polarization ratio does not change with temperature. Generally, there is no ionic polarization in polymer matrix wave-transparent composites. And the interface between the reinforced fibers and polymer matrix is prone to interfacial polarization. If the reinforced fibers present poor interfacial compatibility with polymer matrix, carriers accumulate at the interface of the two-phase (reinforced fibers and polymer matrix) or are trapped by defects, which increases the interfacial polarization, and further causes multiple reflections and losses of electromagnetic wave at the interface (Fig. 5), leading to an increase of tanδ, and reduction in the T of polymer matrix wave-transparent composites [51]. Therefore, desigining polymer matrix wave-transparent composites with low ϵ and tanδ can be realized through either by reducing the polarization molecular density and polarization ratio of reinforced fibers and polymer matrix, or by improving the interfacial bonding strength of the composites.

4. Polymer matrix of wave-transparent composites

Polymer matrix is a host material that realizes the functional characteristics of polymer matrix wave-transparent composites [52], which needs to possess excellent mechanical properties, environmental resistance, thermal stability, and low ϵ and tanδ. Table 1 shows the main properties of the common polymer matrix [53–55].

4.1. Types of the polymer matrix

4.1.1. Epoxy resin

Epoxy resin is one of the most common polymer matrix for wave-transparent composites due to excellent bonding peformance, wear & chemical resistance, low thermal expansion coefficient, and mature curing process [56,57]. In the 1980s, epoxy-based wave-transparent composites were already applied in the radome of the US submarine-launched "Tomahawk" cruise missile. However, epoxy resin presents low heat resistance and cannot meet the heat resistance requirements of aircraft under high Mach number condition. It is currently only used for the radome of subsonic aircrafts and civil aviation aircrafts. Moreover, epoxy resin possesses relatively larger ϵ & tanδ, and poor mechanical properties [58]. Xu et al. [59] designed and synthesized the imidazolium diphenylphosphinate (IDPP) which was then blended with bisphenol A epoxy resin (DGEBA) to prepare modified IDPP/DGEBA resins. The glass transition temperature (T_g) of IDPP/DGEBA resins was significantly improved while ensuring the excellent dielectric properties (ϵ of 4.00 and tanδ of 0.004). When the amount of IDPP was 15 wt%, the T_g of IDPP/DGEBA resins increased from 138.5 °C (pure DGEBA resin) to 172.7 °C. Weng et al. [60] synthesized a redistributed polyphenylene oxide (rPPO) to modify epoxy resin. Modified epoxy resin presented lower ϵ (3.76) and tanδ (0.0021), and the 50 wt% thermal weight loss temperature (T_{50}) was 421.0 °C, 55.9 % higher than that of pure epoxy resin. In addition, Zhou et al. [61] fabricated a hydroxyl-terminated polybutadiene liquid rubber (HTPB) modified epoxy resin (HTPB-epoxy) with low ϵ & tanδ, and excellent mechanical properties. When the amount of HTPB was 10 wt%, the ϵ of the HTPB-epoxy resin reduced from 4.53 (pure epoxy resin) to 4.24, and the tanδ remained low (about 0.023). Meanwhile, the tensile strength and impact strength of the HTPB-epoxy resin were 67.3 MPa and 16.2 kJ/m^2, respectively, higher than those of pure epoxy resin (65.2 MPa and 8.6 kJ/m^2).

4.1.2. Phenolic resin

Phenolic (PF) resin presents excellent mechanical properties, heat & weather resistance, electrical insulation & flame retardant properties, and so on [62,63], and is the polymer matrix originally used in mass production of radomes. In addition, PF resin is commonly used in radomes with high heat resistance requirements. For example, the Sam-6 missile radome and MiG series aircraft

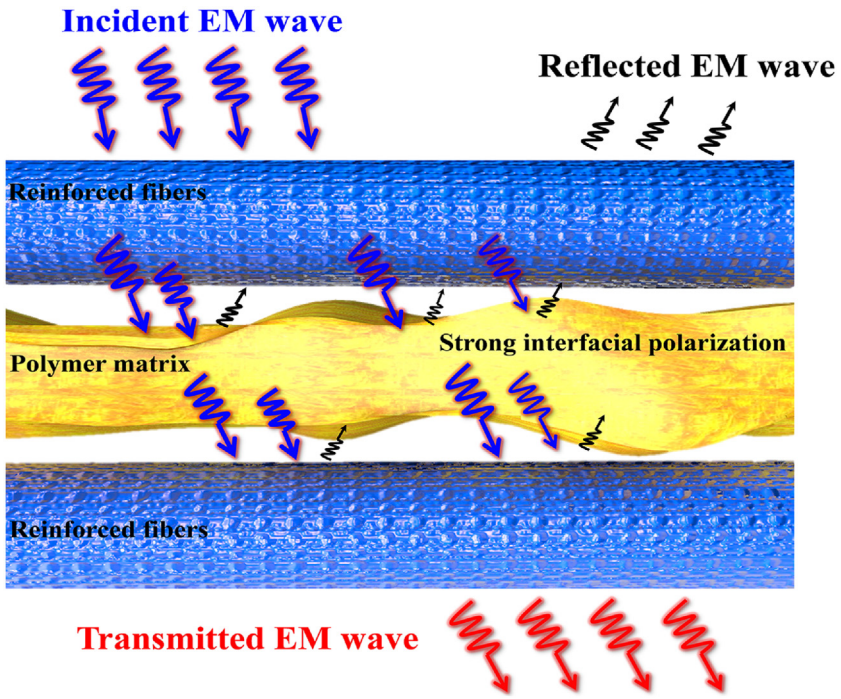

Fig. 5. Schematic diagram of electromagnetic wave transmission at the interface of polymer matrix wave-transparent composites.

Table 1
Main properties of the common polymer matrix.

Polymer matrix	Density (g/cm^3)	Flexural strength (MPa)	Flexural modulus (GPa)	ϵ	tanδ
Epoxy resin (EP)	1.30	97	3.8	3.7–4.1	0.018–0.020
Phenolic resin (PF)	1.30	92	3.5	6.5–8.3	0.015–0.030
Polyimide (PI)	1.40	170	3.8	3.1–3.5	0.005–0.012
Bismaleimide (BMI)	1.30	150	3.7	3.1–3.5	0.005–0.020
Cyanate ester resin (CE)	1.17	80	2.8	2.8–3.2	0.002–0.008
Unsaturated polyester resin (UP)	1.29	85	3.2	2.8–4.0	0.006–0.026
Polytetrafluoroethylene (PTFE)	2.20	90	–	2.1–2.3	0.0003–0.0004
Silicone resin	–	85	–	3.0–5.0	0.003–0.050

radome of the former Soviet Union, and the supersonic shore ship missile radome of China all adopted modified PF resin as polymer matrix. However, PF resin generates low-molecular volatiles during the curing process, resulting in high molding pressure and long post-curing time. Besides, the cured product of the PF resin possesses poor toughness, high ϵ and tanδ. Wu et al. [64] fabricated SiO_2 nanoparticles/*o*-cresol formaldehyde epoxy/boron bisphenol S formaldehyde (BCS) resin with excellent mechanical properties. When the amount of SiO_2 was 6 wt%, the impact strength of the BCS resin increased from 105 to 149 kJ/m^2. And the introduction of SiO_2 had little impact on the dielectric properties of the BCS resin (ϵ of 8.05 and tanδ of 0.0131). Hou et al. [65] synthesized single-crystalline α-Si_3N_4 nanospheres with uniform size (about 50 nm) by using a radio frequency (RF) thermal plasma system *via* a one-step and continuous way. Si_3N_4/PF composites possessed excellent thermal stability (thermal weight loss at 1200 °C was only 17.7 wt%), and lower ϵ (6.0) and tanδ (0.09). However, PF resin is currently rarely used in the high-performance radomes field due to its inherently high ϵ and tanδ values than those of other thermosetting resins (epoxy resin and cyanate resin).

4.1.3. Unsaturated polyester resin

Unsaturated polyester (UP) resin presents simple molding process, low cost, and low ϵ and tanδ. Moreover, UP resin can be cured at room temperature, suitable for large scale production [66]. In the early 1960s, Nan-gatuck Chemical Corporation developed modified UP resin with the trade names of Vibrinl 35 and Vibrinl 36 for the polymer matrix of bomarc missile radomes manufactured by Boeing. However, UP resin possesses poor heat resistance, short storage period, high curing shrinkage, and poor impact strength [67]. Hanemann et al. [68] reported a styrene/UP resin with excellent heat resistance (thermal decomposition temperature of 260 °C), low ϵ (2.6) and tanδ (0.009). It could be potentially used in the fields of aviation, aerospace, and communication services. Dorian et al. [67] fabricated a polybutadiene/UP resin with low ϵ (3.4) and tanδ (0.009), and excellent fracture toughness. The corresponding plane strain fracture toughness of the polybutadiene/UP resin increased from 0.14 MN/m$^{3/2}$ (pure UP resin) to 0.21 MN/m$^{3/2}$. Zhou et al. [69] developed a unique high performance resin by co-polymerizing UP resin with a novel benzyl alcohol terminated hyperbranched polysiloxane (Vi-HPSi). There was little change for ϵ value of Vi-HPSi/UP resin compared to that of pure UP resin, and the tanδ value of Vi-HPSi/UP resin reduced from 0.0315 (pure UP resin) to 0.0196, and the corresponding impact strength increased from 8.2 kJ/m^2 (pure UP resin) to 23.5 kJ/m^2. Chen et al. [70] fabricated a new type of highly heat-resistant modified UP resin by introducing N-phenylmaleimides containing perfluoroalkyl substituents (-CF_3 and -C_6F_{13}). The modified UP resin presented low ϵ (3.63), and the weight loss temperature of 5 wt% (T_5) was 336 °C, higher than that of pure UP resin (327 °C). Sethuraman et al. [71] developed an organic-inorganic hybrid nanocomposites based on vinylsilane-functionalized SBA-15 (VSBA-15) reinforced UP resin. The ϵ value

of obtained VSBA-15/UP resin was 2.4, 79.1 % lower than that of pure UP resin (4.3), and the VSBA-15/UP resin still had excellent heat resistance.

4.1.4. Polyimide resin

Polyimide (PI) resin possesses low ϵ & tanδ, and excellent heat resistance (thermal decomposition temperature is around 500 °C, and T_g is greater than 250 °C) [19,27], which can be used as polymer matrix for radome in the field of aerospace. PMR-15 and AFR-7000 PI resins developed by Nasa Lewis Research Center and Air Force Laboratory in the United States have been widely used in the fields of radomes and high-performance PCB. However, the solvents used to prepare PI resin are usually high boiling points such as N, N'-dimethylformamide (DMF), N, N'-dimethylacetamide (DMAc), and N-methylpyrrolidone (NMP). These solvents are difficult to remove completely during processing, and would easily form holes in the PI resin. In addition, PI resin presents high molecular chain rigidity, poor solubility, and complicated preparation process. Li et al. [72] synthesized 9, 9-bis (3-(3-phenylethynyl) phthalimide-4-hydroxyphenyl) fluorene (Cardo) to be doped into PI resin (PI-Cardo). When the amount of Cardo was 40 wt%, the ϵ of PI-Cardo-40 resin decreased from 3.4 (pure PI resin) to 2.5. Moreover, PI-Cardo-40 resin presented excellent thermal stability and good processability. The T_5 of PI-Cardo-40 resin increased from 459 °C (pure PI resin) to 470 °C. Koytepe et al. [73] adopted the sol-gel method to prepare PI-SiO_2 hybrid composites containing bipyridine. The obtained PI-SiO_2 hybrid composites possessed low ϵ (2.15) and still maintained excellent heat resistance. In addition, Qiu et al. [74] adopted pyromellitic dianhydride (PMDA) as the anhydride monomer and 2, 2-bis (4-(4-(4-aminophenoxy) phenyl) propane) as the amine monomer to prepare PI resin microspheres, which were then doped into PI resin. The ϵ and tanδ of modified PI resin with 50 wt% PI microspheres were 2.2 and 0.0066, respectively, much lower than those of pure PI resin (ϵ, 3.1; tanδ, 0.0233). The tensile strength of modified PI resin increased from 85.8 MPa (pure PI resin) to 128.5 MPa.

4.1.5. Bismaleimide resin

Bismaleimide (BMI) resin possesses fluidity and plasticity similar to that of epoxy resin. In addition, BMI resin presents low moisture absorption rate, high heat resistance, excellent mechanical properties, and low ϵ and tanδ in a wider temperature range, and is widely used in the industrial fields of aerospace, communication services, and electronic information [75,76]. Hexcel P550 and Hexcel F855 type BMI resins developed by American Hexcel Co., Ltd. were used as the polymer matrix for wave-transparent composites. 4501A, 4501B, and 4503 BMI resins developed by Northwestern Polytechnical University present excellent mechanical properties, dielectric properties, and heat resistance, and are also widely used as polymer matrix for wave-transparent composites. However, the cured BMI resin displays high brittleness and poor processability. Yao et al. [77] designed a hollow silica tube (mHST)/bismaleimide (DMA)/diallyl bisphenol A (DBA) resin with excellent mechanical properties, and low ϵ (3.3) and tanδ (0.003). The impact strength of the mHST/DMA/DBA resin was 23.5 kJ/m^2, 119.6 % higher than that of BDM/DBA resin (10.7 kJ/m^2). Chen et al. [78] adopted sulfonated polyether ether ketone (SPEEK), 3, 3′-diallyl bisphenol A (BBA), bisphenol A diallyl ether (BBE), and BMI resin as the raw materials to prepare SPEEK/BBA-BBE-BMI resin by compression molding. When the amount of SPEEK was 5 wt%, the ϵ and tanδ of SPEEK/BBA-BBE-BMI resin decreased from 3.2 and 0.012 (BBA-BBE-BMI resin) to 2.4 and 0.009, respectively. Meanwhile, the flexural strength (147.9 MPa) and impact strength (15.7 kJ/m^2) of SPEEK/BBA-BBE-BMI resin were increased by 49.5 % and 66.2 %, respectively, compared with those of BBA-BBE-BMI resin (flexural strength of 98.9 MPa and impact strength of 9.5 kJ/m^2). Hu et al. [79] developed a new type of mesoporous silica (MPSA)/2, 2′-diallyl bisphenol A (DBA)/4, 4′-bismaleimide diphenylmethane (BDM) resin with improved mechanical and dielectric properties. When the amount of MPSA was 5 wt%, the MPSA/DBA/BDM resin presented low ϵ (3.1) and tanδ (0.015). Compared with that of pure DBA/BDM resin (tensile strength of 160.0 MPa), the tensile strength of MPSA/DBA/BDM resin increased to 187.0 MPa, increased by 16.9 %.

4.1.6. Polytetrafluoroethylene resin

Polytetrafluoroethylene (PTFE) resin is a completely symmetric non-polar linear polymer with very low ϵ and tanδ. In a wide temperature and frequency range, the ϵ of the PTFE resin is stable around 2.1, and the tanδ is about 10^{-4}. In addition, PTFE resin displays excellent chemical resistance, environmental resistance, thermal stability, and low moisture absorption rate (<0.01 %) [80,81]. When PTFE resin is subjected to temperatures above 400 °C, no carbon residue is produced and the ablation products are all volatile compounds, which have little effect on the dielectric properties. Ro3003, TLC-30, Duroid5650, and Avcoat8029 PTFE resins developed by the United States and Russia have been successfully applied in radio systems in the fields of launch vehicles, aircraft, missiles, and return satellites. However, PTFE resin possesses large linear expansion coefficient, poor creep resistance and molding process, which limits its wider application range. Jiang et al. [82] adopted the soft-molding method to prepare the PTFE resin with good dimensional stability (linear expansion coefficient of 1.31 × 10^{-4} m/K) and excellent dielectric properties (ϵ was 2.05 and tanδ was about 10^{-3}). Yuan et al. [83] fabricated γ-aminopropyl triethoxysilane (KH550) modified SiO_2/PTFE resin by powder blending method. When the amounts of KH-550 and SiO_2 were 1.5 and 57 wt%, respectively, KH-550-SiO_2/PTFE resin still maintained excellent dielectric properties (ϵ of 2.70 and tanδ of 0.00135), and the corresponding thermal expansion coefficient reduced from 34.1 ppm/K (pure PTFE resin) to 28.1 ppm/K. Jiang et al. [84] discovered that an appropriate amount of small-sized SiO_2 (2 μm) could fill the pores between large-sized SiO_2 (15 μm), which was beneficial to the formation of a dense microstructure. When the amount of silica of both sizes was 31 wt%, the modified PTFE resin maintained excellent dielectric properties (ϵ of 2.99 and tanδ of 0.002), and the corresponding thermal expansion coefficient was 18.68 ppm/K, lower than that of pure PTFE resin (26.02 ppm/K).

4.1.7. Silicone resin

Silicone resin possesses low ϵ and tanδ under various harsh environmental conditions [85], and the long-term use temperature of silicone resin is around 250 °C. In Russia, silicone resin has been applied in the radar, missiles, space shuttles, and other fields. However, silicone resin presents small intermolecular forces and low cross-linking densities, resulting in poor heat resistance, weak mechanical properties, low viscosity, and complicated processing molding process. Zhu et al. [86] blended methylhydrogensiloxane (MHSis) and poly(methylphenylvinylsiloxane) (Psi) to prepare MHSis/Psi resin. The heat resistance of the MHSis/Psi resin was significantly improved, and the thermal decomposition temperature increased from 355.7 °C (pure Psi resin) to 382.7 °C on the basis of ensuring the excellent dielectric properties of MHSis/Psi resin (ϵ of 2.95, tanδ of 0.0045). Kim et al. [87] fabricated VHR resin from functionalized poly (dimethylsiloxane) (V), polyvinyl functionalized silicone resin (R) and crosslinking agent (H) by hydrogenated silane addition reaction at high temperatures. VHR resin displayed excellent tensile strength (1.34 MPa), low ϵ (3.33) and tanδ (0.002). Zhang et al. [88] synthesized a new type of ASiR resin from poly (methylphenylvinyl siloxane) (PMPVSi) and hyperbranched polysiloxane (EHFHPSi). When the mass ratio of PMPVSi

to EHFHPSi was 2/1, the ASiR resin presented the lowest ϵ (2.96) and tanδ (0.0003), and excellent thermal stability (initial decomposition temperature was 468 °C).

4.1.8. Cyanate ester resin

Cyanate ester (CE) resin contains two or more cyanate functional groups (—OCN), and possesses the highly symmetrical triazine ring structure (low polarity) after curing. In comparison to UP, BMI, PI, and epoxy resin, CE resin displays better wave transmission efficiency with low dielectric constant (ϵ of 2.6–3.2) and dielectric loss tangent (tanδ of 0.005–0.010) in a wide range of temperatures and frequencies [89,90]. In addition, CE resin presents excellent thermal stability, adhesion, low density, high T_g (240–290 °C), and low moisture absorption rate (<1.5 %) [91]. × 54 and 954-2A CE resins produced by Fiberite and the XU 71787 CE resins produced by Dow Chemical present excellent dielectric and mechanical properties, and are widely used in aircraft radomes. However, CE resin presents large brittleness due to the highly cross-linked triazine ring structure. Cao et al. [92] adopted precipitation polymerization to prepare bisphenol A cyanate (BADCy) resin particles, followed by evenly dispersing in BADCy resin matrix to prepare BADCy self-reinforced composites. Compared with that of pure BADCy resin, the tensile strength, flexural strength, and impact strength of BADCy composites increased by 98.1 %, 40.2 %, and 85.4 %, respectively. In addition, BADCy composites presented extremely low ϵ (1.7, much lower than that of pure BADCy resin), and the tanδ remained at low value (0.005). Gao et al. [93] developed a polyphenylene ether (PPO)/BADCy resin with low ϵ (3.3) and tanδ (0.004), and excellent mechanical properties. Compared with that of pure BADCy resin (9.8 kJ/m^2), the impact strength (18.1 kJ/m^2) of PPO/BADCy resin increased by 84.7 %. In addition, Sun et al. [94] developed a modified aluminum phosphate ($AlPO_4$-KH-550)/CE resin with low ϵ (3.10) and tanδ (0.0080), and excellent mechanical properties (the storage modulus of $AlPO_4$-KH-550/CE resin increased from 2210 MPa (pure CE resin) to 2600 MPa.

4.2. Synchronous improvement of dielectric properties and heat resistance of polymer matrix

The dielectric properties and heat resistance of polymer matrix affect the T and using temperature range of polymer matrix wave-transparent composites. At present, there are two main ways to reduce the ϵ and tanδ of polymer matrix. One is to reduce the density of polarized molecules of polymer matrix by reducing the packing density of the internal structure, thereby reducing the ϵ and tanδ of the polymer matrix. The other is to introduce strong electronegative elements to reduce the effect of the applied electric field on electrons to decrease the polarizability of polymer matrix, thereby reducing the ϵ and tanδ [95,96]. In addition, the main method to improve the heat resistance of polymer matrix is to introduce heat-resistant molecular skeleton or nanoparticles into the polymer matrix [97]. However, only improving the dielectric properties or heat resistance of polymer matrix has been unable to meet the low ϵ and tanδ, and high heat resistance requirements of polymer matrix wave-transparent composites.

The cage skeleton structure of polysilsesquioxane (POSS) is highly symmetrical, and the Si—O and SiC— bonds exhibit low ϵ and tanδ due to their low polarity. The bond energy of the Si—O and SiC bonds is much higher than those of CC and CO—— bonds, enduing POSS excellent thermal stability [98]. Lei et al. [62] introduced epoxy-based POSS (EP-POSS) into phenolic novolac (EN) resin to prepare a new type of organic-inorganic hybrid resin (ENH). Compared with those of pure EN resin (ϵ of 6.42 and tanδ of 0.1725), ENH resin with 2 wt% EP-POSS presented lower ϵ (4.11) and tanδ (0.0725). Meanwhile, the T_g of ENH resin increased from 135.4 °C (pure EN resin) to 192.5 °C, T_5 increased from 328.0 °C (pure EN resin) to 340.0 °C. Zeng et al. [99] combined incompletely condensed POSS (TAP-POSS) containing allyl groups, DBA and BDM resin *via* copolymerization to prepare modified BDM resin (BDM/DBA/TAP-POSS). When the amount of TAP-POSS was 3 wt%, the ϵ of BDM/DBA/TAP-POSS resin decreased from 5.94 (BDM/DBA resin, 1 Hz, 250 °C) to 4.39 (1 Hz, 250 °C), and the T_g increased by 36.0 °C. Zhang et al. [100] adopted octa(aminopropyl)silsesquioxane (POSS-NH_2) to modify CE resin. When the amount of NH_2-POSS was 1 wt%, the ϵ and tanδ of POSS-NH_2/CE resin were 2.82 and 0.0032, respectively, lower than the ϵ (3.05) and tanδ (0.0080) of pure CE resin. And the T_g of POSS-NH_2/CE resin (1 wt% NH_2-POSS) increased from 268.0 °C (pure CE resin) to 311.0 °C. Birtane et al. [101] fabricated a series of polyimide (PI) nanocomposites containing [3-(2-aminoethyl)amino]propyl-heptaisobutyl substituted polyhedral oligomeric silsesquioxane (AHIP). When the amount of AHIP was 5 wt%, the ϵ of AHIP/PI resin decreased from 8.6 (pure PI resin) to 5.5, and the T_g of AHIP/PI resin increased from 264.0 °C (pure PI resin) to 284.0 °C.

Adamantane (AMT) and cyclodextrin possess the cage structure similar to POSS, and are also widely used to improve the dielectric properties and heat resistance of polymer matrix due to the rigidity and low polarity [102]. Miao et al. [103] modified graphene oxide (GO) with AMT through the diimide-activated amidation reaction, followed by fabricating GO/AMT-CE hybrid composites. When the amount of GO/AMT was 1 wt%, the ϵ and tanδ of GO/AMT-CE hybrid composites were 2.54 and 0.0063, lower than the ϵ (3.94) and tanδ (0.0122) of pure CE resin, respectively, and the T_5 of GO/AMT-CE hybrid composites increased from 403 °C (pure CE resin) to 431 °C. Tsai et al. [104] designed and synthesized a novel adamantane epoxy resin (ADEP) with low ϵ (3.07, 15.4 % lower than that (3.63) of pure epoxy resin) and excellent heat resistance. In addition, Tang et al. [105] synthesized a cyclodextrin microsphere (M-CDP), followed by doped into CE resin to prepare M-CDP/CE resin. When the amount of M-CDP was 5 wt%, the ϵ of M-CDP/CE resin decreased from 3.40 (pure CE resin) to 2.92. Meanwhile, the initial thermal decomposition temperature of M-CDP/CE resin increased from 368 °C (pure CE resin) to 376 °C. In our previous work, Gu et al. [106] synthesized a novel fluorine/adamantane containing compounds (AEAF) from bisphenol AF, 1-adamantyl chloride, and epichlorohydrin (ECH) through successive esterification and O-alkylation reaction, which was then introduced into the curing networks of BADCy resins *via* copolymerization to obtain AEAF-*co*-BADCy resins (Fig. 6). When the amount of AEAF was 6 wt%, AEAF-*co*-BADCy resins displayed the minimum values of real part (ϵ'_r), imaginary part (ϵ''_r) of complex permittivity, and tanδ, which were 2.49, 0.012, and 0.0048, respectively (at 10 GHz), and much lower than those of pure BADCy (ϵ'_r of 2.93, ϵ''_r of 0.019 and tanδ of 0.0065, 10 GHz). Meanwhile, it presented the optimal thermal stability (heat resistance index (T_{HRI}) of 217.9 °C) and the highest T_g (276.3 °C), increased by 5.1 % and 8.7 %, respectively, compared with those of pure BADCy resins (T_{HRI} of 207.3 °C and T_g of 254.1 °C).

Fluorine (F) is the most electronegative element, and fluorine-containing molecules present low polarizability [95]. Therefore, the introduction of C—F bond is favor of reducing the ϵ and tanδ of polymer matrix. Moreover, the introduction of C—F bond can also improve the heat resistance of the polymer matrix due to high binding energy of C—F [107]. Yuan et al. [108] adopted the perfluorocyclobutyl (PFCB) aromatic ether polymer to modify silicone resin (Si-PFCB). The ϵ and tanδ of Si-PFCB resin were 2.33 and 0.0021, respectively, much lower than those of the silicone resin reported in other literatures (ϵ, 3.0–5.0; tanδ, 0.003–0.050). Meanwhile, Si-PFCB resin possessed high thermal stability, the T_5 was 472 °C, and the T_g was greater than 350 °C. Chen et al. [109] designed and synthesized a fluorine-containing polymer with amino groups in the side chain (PFNP) to modify epoxy resin. PFNP participated in the curing reaction of epoxy resin and was evenly dispersed in the

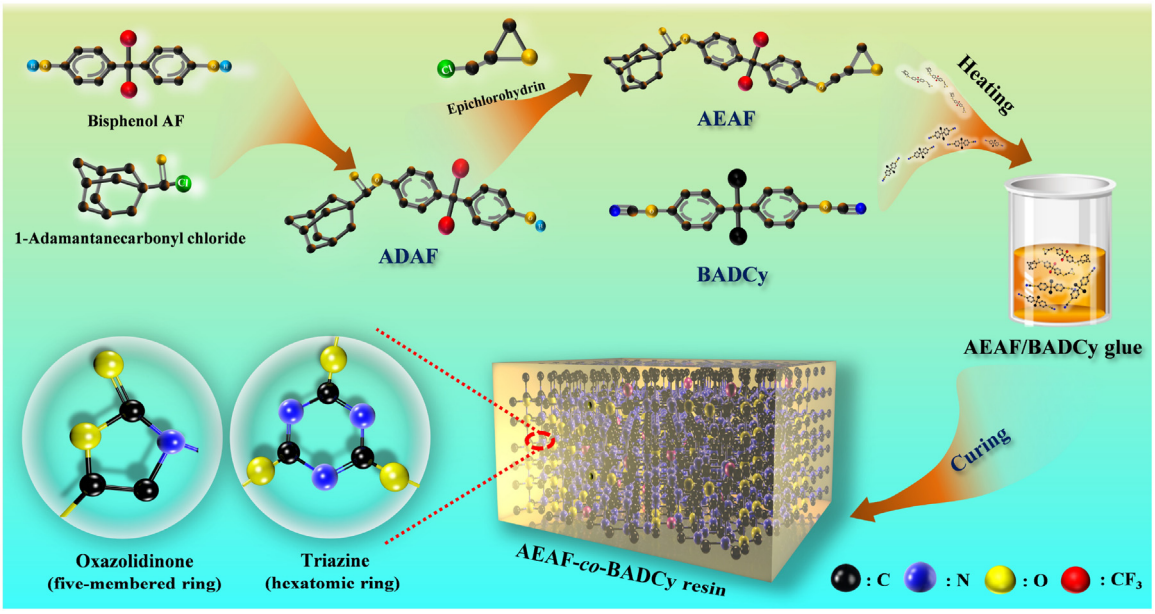

Fig. 6. Schematic diagram of preparation of AEAF-*co*-BADCy resins. Reprinted with permission from Ref. [106]. Copyright (2020) Elsevier Ltd.

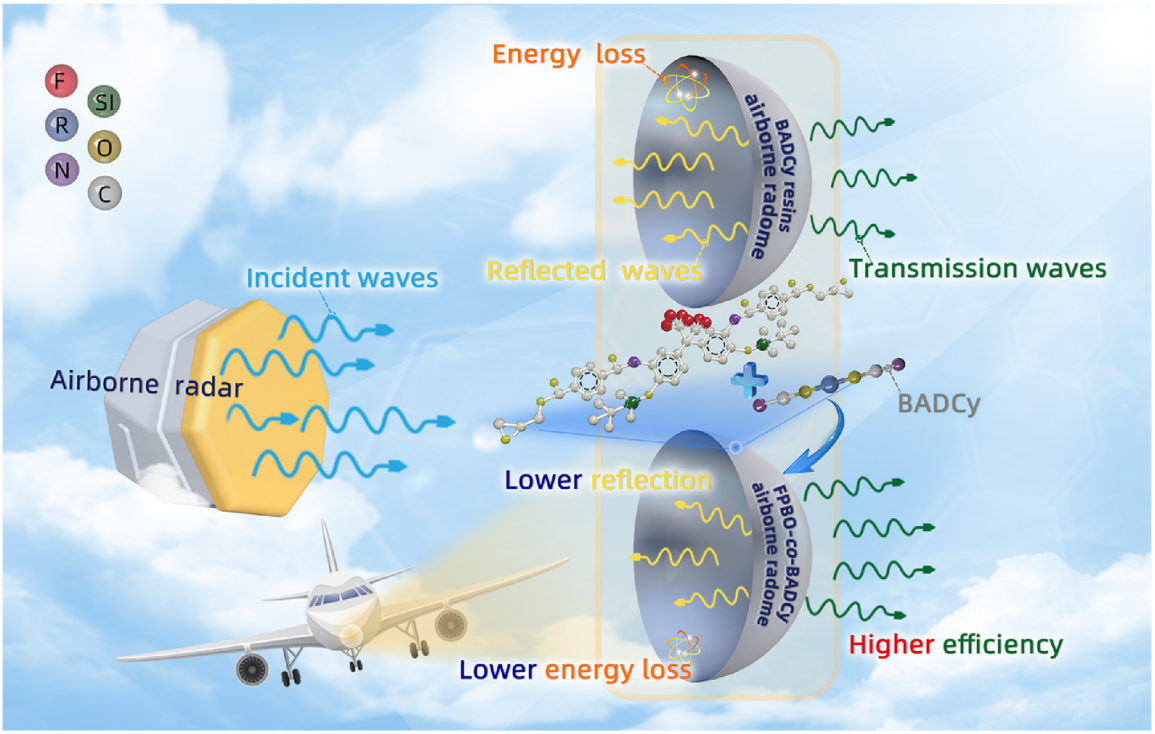

Fig. 7. Schematic diagram of electromagnetic wave transmission mechanism for FPBO-*co*-BADCy resins. Reprinted with permission from Ref. [110]. Copyright (2019) Elsevier Ltd.

epoxy resin. When the amount of PFNP was 10 wt%, the ϵ of EP-10 resin was 3.5, much lower than that of pure epoxy resin (5.4), and the T_g of EP-10 resin increased from 156.1 °C (pure epoxy resin) to 175.1 °C. In addition, Jiang et al. [90] synthesized a novel bisphenol 3,5-bis(trifluoromethyl)phenylhydroquinone (BTFMHQ) and the corresponding modified epoxy resin (BTFMEP) *via* multi-step procedure including the Meerwein arylation reaction, followed by nucleophilic reaction. Compared with those (ϵ of 3.01 and tanδ of 0.0139) of commercially available DGEBA, BTFMEP presented lower ϵ (2.59) and tanδ (0.0114), and excellent thermal stability (T_g of 142 °C). In our previous work, Gu et al. [110] synthesized the fluorine-containing epoxy-terminated PBO precursor (epoxy-preFPBO) from 2, 2-bis(3-amino-4-hydroxyphenyl) hexafluoropropane (6FAP) and terephthaloyl chloride (TPC) *via* condensation reaction followed by end-group functionalization with glycidol. Afterwards, epoxy-preFPBO modified CE resins (FPBO-*co*-BADCy resins, Fig. 7) were prepared by copolymerization of epoxy-preFPBO and BADCy resin. FPBO-*co*-BADCy resins with 7 wt% epoxy-preFPBO displayed the optimal wave-transparent performances. The ϵ and tanδ were 2.48 and 0.0081, respectively, lower than those of pure BADCy (ϵ of 3.05, tanδ of 0.0090). Moreover, FPBO-*co*-BADCy resin possessed excellent thermal stability

(T_5 was 375.2 °C), which was a very promising polymer matrix for radomes.

In addition, the cross-linking of different polymers could form an interpenetrating polymer network (IPN), and the macromolecular chains of polymer matrix are intertwined and penetrated through each other in the curing network to refine the microstructure, thereby improving the compatibility between polymer matrix [111,112]. Furthermore, the introduction of molecular chains with low polarity in the curing network can effectively constrain the orientation and relaxation of polar molecular chains, thereby reducing the ϵ and tanδ. Moreover, the interpenetrating network presents high stability and excellent heat resistance [113]. For example, the bismaleimide triazine (BT) resin fabricated by BMI and CE resin possesses the excellent performance: low ϵ (3.0–3.5), high T_g (190−290 °C), low water absorption (0.2–2.5 wt%), and excellent dimensional stability and processability. Hwang et al. [114] adopted BMI, 2, 6-dimethylphenol-dicyclopentadiene dicyanate (DCPDCY), and 2, 6-dimethylphenol-dipentene dicyanic acid ester (DPCY) to prepare a series of BT resins with low ϵ (2.53) and excellent thermal stability (T_5 is 445 °C). In addition, Jie et al. [115] fabricated DBA/BT hybrid resin. The ϵ of DBA/BT resin was reduced from 3.07 (BT resin) to 2.91, and the thermal decomposition temperature exceeds 400 °C. Guo et al. [116] fabricated the fluorine-containing BT resin from 2, 2′ -bis (4-cyanophenyl) propane (CY-1), 2′ -bis (4- (4-maleimide oxy) phenyl) hexafluoropropane (6FBMP), and diallyl hexafluorophthalol A (6FDABPA). The ϵ and tanδ of fluorine-containing BT resin were 2.89 and 0.002, respectively, much lower than the reported CE and BMI resins. And the fluorine-containing BT resin presented excellent thermal stability (the T_g was 220 °C, and the T_5 was around 400 °C). Tu et al. [117] synthesized a new type of diphenyl ether-containing phenolic resin (MPF), followed by copolymerizing with BADCy resin to prepare MPF/BADCy resin. When the amount of MPF was 30 wt%, the ϵ and tanδ of MPF/BADCy resin were 3.00 and 0.0062, respectively, lower than the ϵ (3.2) and tanδ (0.0080) of BADCy resin reported in other literatures. Meanwhile, MPF/BADCy resin still presented excellent thermal stability.

5. Reinforced fibers of polymer matrix wave-transparent composites

Reinforced fibers for polymer matrix wave-transparent composites are mainly divided into inorganic and organic fibers [118–122]. Table 2 shows the physical and chemical properties of common reinforced fibers.

Reinforced fibers generally possess high specific strength/modulus, lower density, low ϵ and tanδ. However, the structure of reinforced fibers is highly ordered along the fiber axis, resulting in a chemically inert surface and poor interfacial compatibility with polymer matrix [123–126]. Therefore, a large number of defects are likely to occur at the interface between reinforced fibers and polymer matrix (Fig. 8). To our knowledge, increasing the surface activity of reinforced fibers by surface functionalization is beneficial to the interfacial compatibility between the reinforced fibers and polymer matrix, thereby reducing the interfacial polarization, and improving the interfacial bonding strength and other related mechanical properties of polymer matrix wave-transparent composites.

5.1. Inorganic fibers

5.1.1. Glass fibers (GFs)

GFs are the earliest and most widely used reinforced fibers in radomes due to their low cost, low ϵ and tanδ, excellent insulation properties and mechanical properties [127–130]. In the 1950s, the Boeing Company successfully applied the radome made of GFs to the main guided missile (3 Mach).

At present, E, S, D-GFs are main reinforced fibers of polymer matrix wave-transparent composites [131–133]. E-GFs with low cost, also known as alkali-free GFs, are currently the most widely used GFs. S-GFs are mainly composed of oxides such as magnesium, aluminum, silicon, *etc*, and mainly used in military and other fields because of the expensive cost, high strength and elasticity. The ϵ and tanδ of D-GFs are the lowest of the three, suitable for the fields with higher requirement on the wave transmission. For example, D-GFs are used in the radomes of the US Hawk missile and SA-6 missile of the former Soviet Union. However, the mechanical properties of D-GFs are relatively poor, only 70 % of E-GFs, which limits their wider application [134,135].

However, the chemical composition of GFs is very different from that of polymer matrix [136,137]. It is necessary to adopt appropriate methods to improve the interfacial compatibility of GFs and polymer matrix. At present, researchers mainly improve the interfacial compatibility of GFs and polymer matrix through two aspects. On the one hand, GFs are treated to eliminate impurities or weak boundary layer on the surface, so as to improve the infiltration with polymer matrix. On the other hand, active groups are introduced on the surface of GFs to react with polymer matrix, to form an interfacial phase connected by chemical bonds. The common surface functionalization methods of GFs mainly include plasma treatment, acid etching, coupling agent treatment, chemical grafting modification, and surface coating [138–140].

Plasma treatment mainly relies on high-energy plasma to change the chemical composition of GFs' surface [141–143]. The electron in the plasma has high enough energy to break the chemical bond, thereby destroying the chemical structure of the surface and improving the surface activity of GFs. Meanwhile, plasma treatment slightly etched the surface of GFs, increased the contact area of GFs and polymer matrix, and further improved the interfacial bonding strength of GFs reinforced composites. Researchers usually adopt low-temperature plasma to functionalize GFs to avoid the destruction of GFs structure by high temperature. Lim et al. [144] found that GFs treated by low-temperature oxygen plasma presented smaller contact angle and higher surface energy. And excess water and residues of GFs were removed during the treatment, resulting in a reduction in the ϵ of the functionalized GFs. Ihara et al. [145] adopted low-temperature NH_3 plasma to treat GFs. Compared with that of pure GFs reinforced plastic (205.4 MPa), the tensile strength (237.2 MPa) of the functionalized GFs reinforced plastic (GFRP) increased by 15.5 %. Zhang et al. [127] applied air plasma to improve the interfacial adhesion between GFs and adhesive for preparing GFs reinforced laminated veneer lumber (LVL) composites with excellent mechanical properties. Compared with those of pure LVL composites, the modulus of rupture and elasticity values of plasma-modified LVL composites increased by 36.0 % and 16.0 %, respectively. Kusano et al. adopted helium plasma to treat GFs. The surface energy of functionalized GFs increased from 20 mJ/m^2 (pure GFs) to 80 mJ/m^2. However, plasma treatment equipment possesses high requirements, complicated operation, and is difficult for industrialization.

The principle of acid etching is to dissolve Al_2O_3, MgO, and Na_2O of GFs, resulting in the formation of depressions and micropores on the surface, which plays an anchoring role and is beneficial to adhering to the polymer matrix. In addition, the acid can react with SiO_2 of GFs to form a large amount of silanol, further improving the interfacial bonding strength between GFs and polymer matrix [146,147]. The functionalization effect of acid etching on GFs is mainly related to the type and concentration of acid, treatment time, and temperature. Too high acid concentration and too long treatment time would lead to the destruction of the GFs structure. Tomao et al. [148] found that the functionalized GFs

Table 2
Physical and chemical properties of common reinforced fibers.

Fibers	Properties				
	Density (g cm^{-3})	Tensile strength (GPa)	Modulus (GPa)	ϵ (1 MHz)	tanδ (1 MHz)
E-glass fibers	2.54	3.75	72	6.13	0.0038
S-glass fibers	2.49	4.00	85	5.21	0.0068
D-glass fibers	2.60	2.40	52	4.00	0.0025
Quartz fibers	2.20	1.70	72	3.78	0.0002
Basalt fibers	2.80	3.50	80	2.63	0.0050
Kevlar 49 fibers	1.45	3.45	137	3.85	0.0010
UHMPE fibers	0.97	5.01	193	3.00	0.0001
PBO fibers	1.56	5.80	280	3.00	0.0010

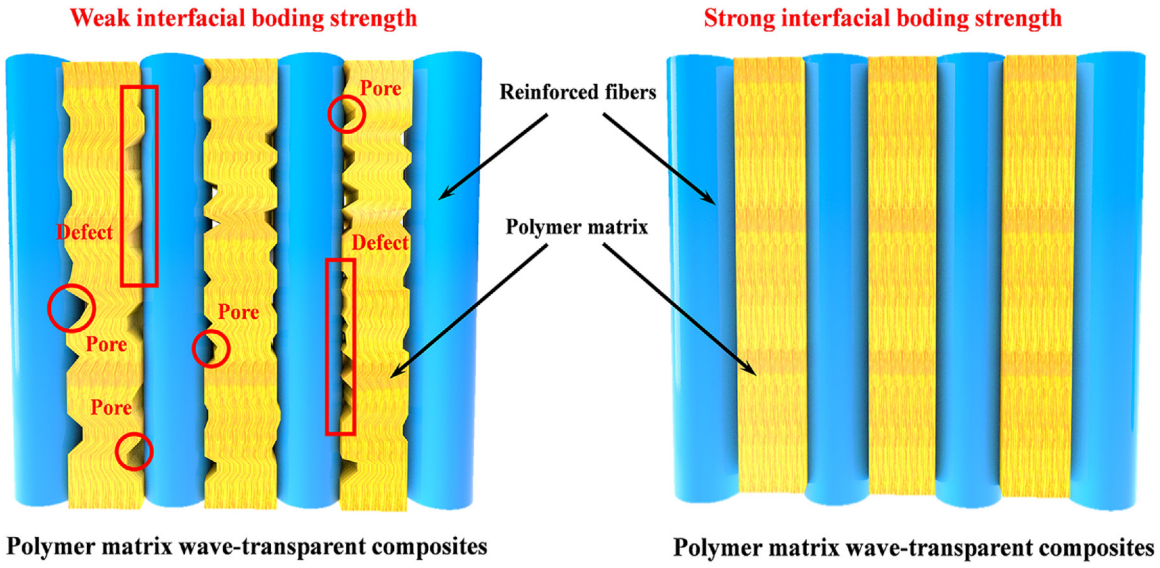

Fig. 8. Schematic diagram of interfacial defects for polymer matrix wave-transparent composites.

obtained by treatment with 20 % HCl for 6 h at 100 °C displayed the highest content of silanol under the premise that the structure of GFs is not destroyed. Cho et al. [149] found that applying 20 % H_2O_2 and 80 % H_2SO_4 mixed acid to treat S-GFs for 24 h could obtain functionalized GFs with the highest surface activity (Gr- (iii) GFs). And the interlaminar shear strength (ILSS) of Gr-(iii) GFs/polyurethane dimethacrylate composites increased from 7.38 MPa (pure GFs/polyurethane dimethacrylate composites) to 10.30 MPa, increased by 39.6 % (Fig. 9(a)). Arunprakash et al. [150] adopted H_2SO_4 and NaOH to successively treat GFs. Compared with that of pure GFs/epoxy resin composites, the ILSS of functionalized GFs/epoxy composites increased by 12.5 %. Karunagaran et al. [151] dipped GFs in H_2SO_4 for 24 h to obtain functionalized GFs and found that the flexural strength of the functionalized GFs/epoxy composites increased from 309 MPa (pure GFs/epoxy resin) to 380 MPa.

Coupling agent treatment is the most commonly applied surface functionalization methods of GFs, among which silane coupling agent is the most widely used [152]. The silane coupling agent reacts with the silicon hydroxyl groups on the surface of GFs to form a stable Si-O-Si structure, thereby improving its surface activity. The corresponding silane coupling agent should be selected according to different polymer matrix. Park et al. [153] functionalized GFs with methacryloxypropyltrimethoxysilane (KH-570), which was then applied to prepare functionalized GFs/unsaturated polyester composites. The ILSS of the functionalized GFs/unsaturated polyester composites increased from 16.2 MPa (pure GFs/unsaturated polyester composites) to 27.4 MPa. Sever et al. [154] adopted 3-(2, 3-epoxypropyloxy) propyltrimethoxysilane (KH-560) to functionalize GFs. Compared with that of pure GFs/epoxy composites, the ILSS of functionalized GFs/epoxy composite increased by 59 %. In addition, Sever et al. [155] found that if the treatment time of the silane coupling agent was too long, a thick coupling agent layer would be formed on the surface of the GFs, which made the contact angle of functionalized GFs larger, resulting in poor wettability with polymer matrix. Nigel et al. [156] adopted aminopropyltrimethoxysilane (APS) and KH-560 to functionalize the surface of GFs. The ILSS of KH-560-GFs/PF composites was 78.4 % higher than that of APS-GFs/PF composites.

Chemical grafting functionalization is usually combined with the coupling agent treatment, and the functional groups of the coupling agent are usually used for secondary functionalization to make the surface-active group and molecular chain segments more abundant, further improving the interfacial compatibility with polymer matrix. In addition, the biggest advantage of chemical grafting functionalization is that it can graft specific active groups on the surface of GFs according to the structure of polymer matrix, to significantly improve the interfacial bonding strength of the obtained composites. Li et al. [157] synthesized triblock copolymer coupling agent polystyrene-block-poly(n-butylacrylate)-*block*-poly(c-methacryloxypropyltrimethoxysilane), (PS-*b*-PnBA-*b*-PMPS) by atom transfer radical polymerization, which was then chemically grafted on the GFs surface. The functionalized GFs presented better interfacial compatibility with polyethylene, and the ILSS of the functionalized GFs/polyethylene composites increased from 4.9 MPa (pure GFs/polyethylene) to 17.7 MPa. In addition, Zhang et al. [158] grafted polymer brushes (PMMA or PS) on the surface of GFs

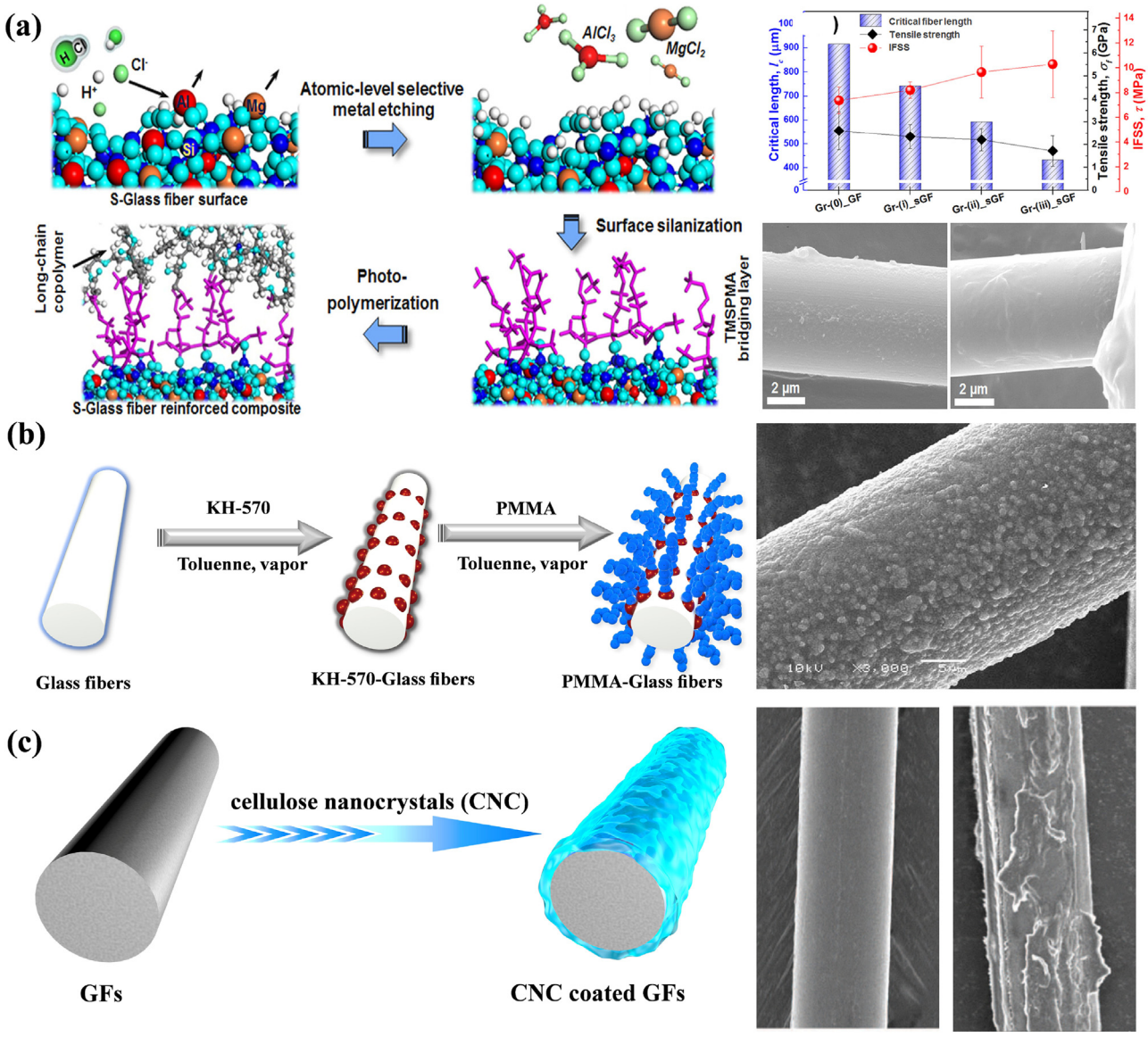

Fig. 9. Schematic diagram of acid etching process on S-GFs (a). Reprinted with permission from Ref. [149]. Copyright (2019) American Chemical Society; Schematic diagram of preparation for PMMA-GFs and their SEM images (b). Reprinted with permission from Ref. [158]. Copyright (2010) Wiley-vch Verlag GmbH & Co. KGaA, Weinheim; Schematic diagram of preparation for CNC coated GFs and their SEM images (c). Reprinted with permission from Ref. [160].

pretreated by KH-550, and the surface roughness of the functionalized GFs was greatly improved (Fig. 9(b)). What's more, acid treated GFs presented a large number of silanol groups, which could also be used for secondary functionalization. Tao et al. [159] grafted hydroxyl-terminated poly-*n*-butyl acrylate-b-styrene (HO-P (BA-bS)) onto the surface of GFs pretreated by H_2SO_4. The ILSS of the functionalized GFs/polystyrene composites increased from 8.5 MPa (pure GFs/polystyrene) to 14.9 MPa.

Surface coating refers to coating a layer containing polar groups, to enhance the surface roughness and introduce active groups on the surface of GFs, thereby strengthening the interfacial bonding strength between GFs and polymer matrix through mechanical engagement or chemical bonding. Surface coating presents simple operation, mild conditions, and none destruction to the performance of GFs. Asadi et al. [160] functionalized the surface of GFs with cellulose nanocrystals (CNC), followed by preparing CNC coated GFs/epoxy composites. When the amount of CNC was 0.17 wt%, the elastic modulus and tensile strength of CNC coated GFs/epoxy composites increased by 10 %, and the corresponding flexural modulus and flexural strength increased by 40 % and 43 % (Fig. 9(c)) respectively, compared with those of pure GFs/epoxy composites. Nygard et al. [161] built a polypropylene/maleic anhydride coating (PP-*g*-MAH) on the surface of GFs, which significantly improved the ILSS of PP-*g*-MAH/GFs/PP composites. The ILSS of the PP-*g*-MAH/GFs/PP composites increased from 6.6 MPa (pure GFs/PP composites) to 20.2 MPa. In addition, He et al. [162] designed ternary multi-scale hybrid coatings (nano Al_2O_3, micro Al_2O_3, and short carbon fiber (SCF)) to functionalize GFs. Compared with that of GFs reinforced polymer (GFRP), the type II interlaminar fracture toughness of functionalized GFRP increased by 38.2 %. In our previous work, Gu et al. [163] employed silica-sol, synthesized from tetraethyl orthosilicate (TEOS) and KH-560 *via* sol-gel method, to functionalize the surface of GFs (Si-GFs). The flexural strength (539.6 MPa) and ILSS (34.8 MPa) of the Si-GFs/epoxy resin laminated composites respectively increased by 15.5 % and 24.7 %, compared with those (flexural strength of 467.1 MPa and ILSS of 27.9 MPa) of pure GFs/epoxy resin laminated composites.

5.1.2. Quartz fibers

Quartz fibers are currently the most used reinforced fibers for polymer matrix wave-transparent composites due to their excellent ablation resistance, impact resistance, outstanding chemical stability, and ultralow ϵ and tanδ (the tanδ is much lower than that of GFs) [164–166]. In addition, quartz fibers can be used for a long time at about 1050 °C, and the instantaneous heat resistance temperature can reach 1700 °C, which is very suitable for radomes in the aerospace and missile fields. However, the bare quartz fibers present relatively poor mechanical properties. Coating a layer of sizing agent on the surface of quartz fibers during the generation process is in favor of repairing its surface defects, thereby improving the strength of quartz fibers.

Surface functionalization methods of quartz fibers are basically similar to those of GFs. Wang et al. [167] adopted two silane coupling agents (KH-550 and KH-570) to functionalize the surface of quartz fibers. KH-550 functionalized quartz fibers presented better interfacial compatibility with bisphenol A-glycidyl dimethacrylate (bis-GMA). The corresponding flexural strength of functionalized quartz fibers/bis-GMA composites increased from 270.9 MPa (pure quartz fibers/bis-GMA) to 620.3 MPa. Luo et al. [168] fabricated functionalized quartz fibers pretreated by KH-550. The tensile strength and impact strength of the functionalized quartz fibers/PMMA composites increased by 13 % and 43 %, respectively, compared with those of the pure quartz fibers/PMMA composites. Ge et al. [169] utilized a silane coupling agent (AG-2) containing terminal alkyne to functionalize the surface of the quartz fibers. Compared with those of the quartz fibers/PSA resin composites, the ILSS and flexural strength of the functionalized quartz fibers/PSA resin composites increased by 34.77 % and 38.30 %, respectively. Zhang et al. [170] synthesized vertically aligned carbon nanotubes (VA-CNT) composed of multi-walled carbon nanotubes (MWCNT) on the surface of quartz fiber fabrics using plasma-enhanced chemical vapor deposition to prepare VA-CNT functionalized quartz fiber fabrics. The contact angle of VA-CNT functionalized quartz fiber fabrics with distilled water decreased from 96.5° (pure quartz fiber fabric) to 30.6° (Fig. 10(a)).

5.1.3. Basalt fibers

Basalt fibers possess excellent tensile strength, high flame retardancy, ablation resistance, wear resistance, low ϵ and tanδ, *etc.* Compared with GFs, basalt fibers present simple preparation process, lower cost, and is the only non-carcinogenic, environmentally friendly green high-performance fibers so far [171,172]. At present, the application of basalt fibers in the polymer matrix wave-transparent composites for radomes is still in its infancy.

Basalt fibers present smooth surface, which cannot realize effectively physical or chemical connection to polymer matrix [173–175]. Manikandan et al. [176] used H_2SO_4 to functionalize basalt fibers. The ILSS of the functionalized basalt fibers/UP composites increased by 24.15 %, compared with that of the basalt fibers/UP composites. Liu et al. [177] combined HCl with KH-550 to functionalize the surface of basalt fibers. The impact strength of the functionalized basalt fibers/bisphenol F-type epoxy composites was 77 % higher than that of the pure basalt fibers/bisphenol F epoxy composites. In addition, surface coating can avoid damage to the structure of basalt fibers. Wei et al. [178] constructed an organic/inorganic hybrid coating (epoxy resin/silica hybrid materials) on the surface of basalt fibers. The tensile strength of functionalized basalt fibers was 15 % higher than that of pure basalt fibers. Moreover, the functionalized basalt fibers displayed better interfacial compatibility with bisphenol A epoxy resin. Compared with that of the pure basalt fibers/bisphenol A epoxy resin composites, the ILSS of the functionalized basalt fibers/bisphenol A epoxy composites increased by 10 %. Zhang et al. [179] adopted polyacrylamide/epoxy resin/nano-SiO_2 coating to functionalize the surface of basalt fibers, and functionalized basalt fibers possessed rougher surface and improved hydrophilicity (Fig. 10(b)).

5.2. Organic fibers

5.2.1. Kevlar fibers

DuPont realized the industrialization of poly (p-phenylene terephthalamide) fibers (trade name of Kevlar fibers) in 1972. Kevlar fibers with a highly ordered molecule chain and high crystallinity, present high specific strength/modulus, excellent dimensional stability, chemical & fatigue resistance, low density (1.44 g/cm^3), low ϵ and tanδ, and are mainly applied in thin-walled and flexible deployable radomes [180,181]. However, Kevlar fibers possess high hygroscopicity (easy to cause ϵ to increase in hot and humid environment) and poor UV resistance. In addition, Kevlar fibers present extremely chemically inert and poor interfacial compatibility with polymer matrix. Surface functionalization methods of Kevlar fibers mainly include physical modification, chemical modification, and surface coating [182–185].

The common physical modification methods include plasma treatment, high-energy radiation treatment, and corona treatment. Su et al. [186] used oxygen plasma to functionalize the surface of Kevlar fibers. When the oxygen plasma treatment time and power were 300 s and 60 W, respectively, the functionalized Kevlar fibers/BMI resin composites presented optimal ILSS (161.0 MPa), which increased by 40 %, compared with that of pure Kevlar fibers/BMI resin composites (115.0 MPa). Jia et al. [187] adopted air plasma to treat Kevlar fibers. When the treatment time and power were 12 s and 300 W, respectively, the ILSS (61.7 MPa) of the functionalized Kevlar fibers/poly (phthalazinone ether sulfone ketone) composites increased by 34.1 %, compared with that (46.0 MPa) of Kevlar fibers/poly (hthalazinone ether sulfone ketone) composites. Zhang et al. [188] adopted γ-ray to treat Kevlar fibers, followed by grafting KH-560 on the surface. The ILSS of the functionalized Kevlar fibers/epoxy composites increased from 42.1 MPa (pure Kevlar fibers/epoxy resin composites) to 55.6 MPa. Nejman et al. [189] performed discharge treatment on Kevlar fiber fabrics. The surface free energy of the functionalized Kevlar fiber fabrics increased from 44.06 mJ/m^2 (pure Kevlar fiber fabrics) to 70.01 mJ/m^2. However, the above mentioned surface functionalization methods are likely to destroy the structure of Kevlar fibers themselves, thereby decreasing the mechanical properties.

Chemical grafting modification includes chemical substitution and chemical oxidation. Hydrogen in the ortho- and para-position of the benzene ring in Kevlar fibers can be substituted with certain electrophilic substitution groups. Liu et al. [190] grafted epichlorohydrin to the benzene ring of the surface of Kevlar fibers through the Friedel-Crafts reaction. When the reaction time was 1 h, the functionalized Kevlar fibers presented the best interfacial bonding strength with epoxy resin, and the single fiber pull-out strength of functionalized Kevlar fibers/epoxy resin microcomposites increased from 8.0 MPa (Pure Kevlar fibers/epoxy resin) to 12.1 MPa. Chemical oxidation grafting is to improve the surface roughness and activity of Kevlar fibers with oxidizing chemical reagents. Zhang et al. [191] used nitrification media to pretreat Kevlar fibers, and then grafted hyperbranched polysiloxane (HPSi) onto the surface of Kevlar fibers (HPSi-*g*-Kevlar). HPSi-*g*-Kevlar fibers presented a rougher surface morphology, and its surface free energy was 1.7 times that of pure Kevlar fibers. Lin et al. [192] pretreated Kevlar fibers with bromine water, and then grafted epichlorohydrin on its surface. Compared with that of Kevlar fibers/epoxy resin composites, the ILSS of functionalized Kevlar fibers/epoxy composites increased by 12.0 %. Tao et al. [193] applied the methodology of metalation to pretreat the Kevlar fibers and then grafted alkoxysilane on its surface. The ILSS of the function-

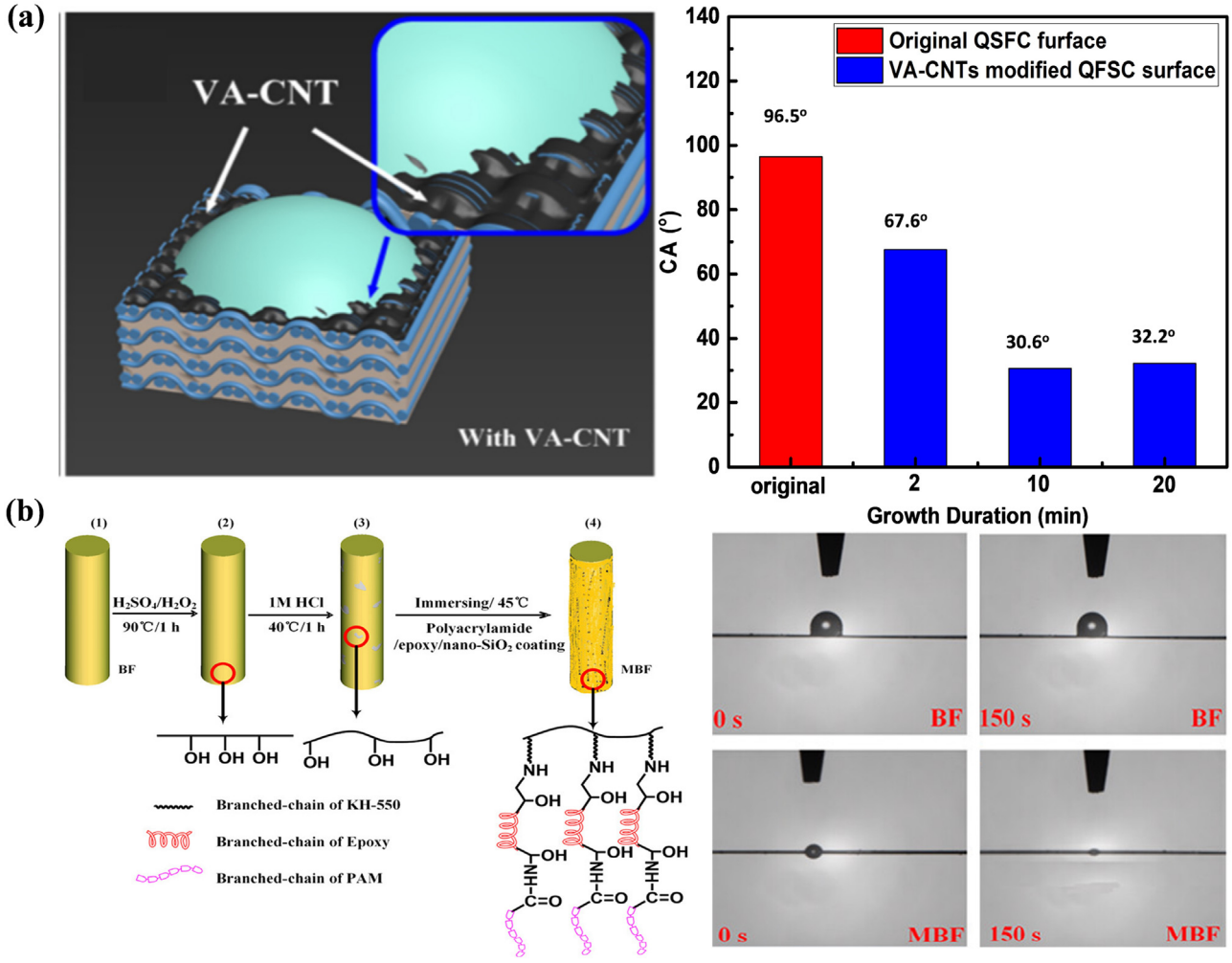

Fig. 10. Schematic diagram of the wetting morphology on the VA-CNT modified quartz fibers fabric surface (a). Reprinted with permission from Ref. [170]. Copyright (2019) Elsevier Ltd. Schematic diagram for the preparation of Polyacrylamide/epoxy/nano-SiO_2 coated basalt fibers (b). Reprinted with permission from Ref. [179]. Copyright (2018) American Chemical Society.

alized Kevlar fibers/epoxy composites was 36.3 MPa, 57.1 % higher than that (23.1 MPa) of pure Kevlar fibers/epoxy composites.

Coating polymers or other highly viscous substances on the surface of Kevlar fibers is in favor of enhancing the interfacial bonding strength between Kevlar fibers and polymer matrix [194,195]. Rodríguez et al. [196] deposited acid-treated oxidized multi-walled carbon nanotubes (MWCNT) on the surface of Kevlar fibers. The number of active functional groups such as —COOH and O—H on the surface of the functionalized Kevlar fibers was greatly increased (Fig. 11(a)). Zhou et al. [197] prepared BL-aramid fibers by alternately self-assembling SiO_2 and MgAlFe layered double hydroxide (LDH) on surfaces of aramid fibers through a green layer-by-layer (LBL) self-assembly technique without using high temperature and organic solvent. The surface energy of BL-aramid fibers was 1.8 times that of pure aramid fibers (Fig. 11(b)). Liang et al. [198] constructed a new hybrid coating with hyperbranched polysiloxane (HSi)/$Ce_{0.8}Ca_{0.2}O_{1.8}$ on the surface of Kevlar fibers by in-situ method (HSi-$Ce_{0.8}Ca_{0.2}O_{1.8}$@Kevlar). The surface free energy of HSi-$Ce_{0.8}Ca_{0.2}O_{1.8}$@Kevlar fibers was 40 % higher than pure Kevlar fibers. Dopamine (DA) can form a polymer network (polydopamine, PDA) through oxidative crosslinking, which firmly adheres to the surface of Kevlar fibers. Rina et al. [199] used DA/KH-560 to functionalize the surface of Kevlar fibers (Kevlar-PDA/KH-560). The ILSS of Kevlar-PDA/KH-560 fibers/rubber composites increased by 61.5 %, compared to pure Kevlar fibers/rubber composites. Fu et al. [184] designed and fabricated DA-coated functionalized Kevlar fibers, which presented better interfacial compatibility with olefin block copolymer (OBC). In our previous work, Gu et al. [200] adopted DA/POSS to functionalize the surface of Kevlar (POSS-*g*-Kevlar@PDA, *f*-Kevlar) cloth. And the ILSS of *f*-Kevlar cloth/BADCy matrix wave-transparent laminated composites increased by 73.7 %, compared with that of pure Kevlar cloth/BADCy matrix wave-transparent laminated composites. Moreover, the low-polarity of POSS reduces the interfacial polarization of the *f*-Kevlar cloth/BADCy matrix wave-transparent laminated composites, further reducing the ϵ and tanδ of the composites (Fig. 11(c)).

5.2.2. Ultra high molecular weight polyethylene (UHMWPE) fibers

UHMWPE fibers possess molecular structure with low polarity and low dispersion, excellent mechanical properties, low density (0.90 g/cm^3, which is the lowest density of reinforced fibers), excellent UV radiation & chemical corrosion resistance, and low ϵ and tanδ [201–203]. However, UHWMPE fibers present low melting point, poor dimensional stability, high surface inertness, and poor interfacial interaction with polymer matrix. At present, the polymer matrix wave-transparent composites of UHMWPE fibers are only in the experimental research stage.

In order to improve the surface activity of UHMWPE fibers, Wang et al. [204] applied tannic acid (TA) and Na^+ to coat the sur-

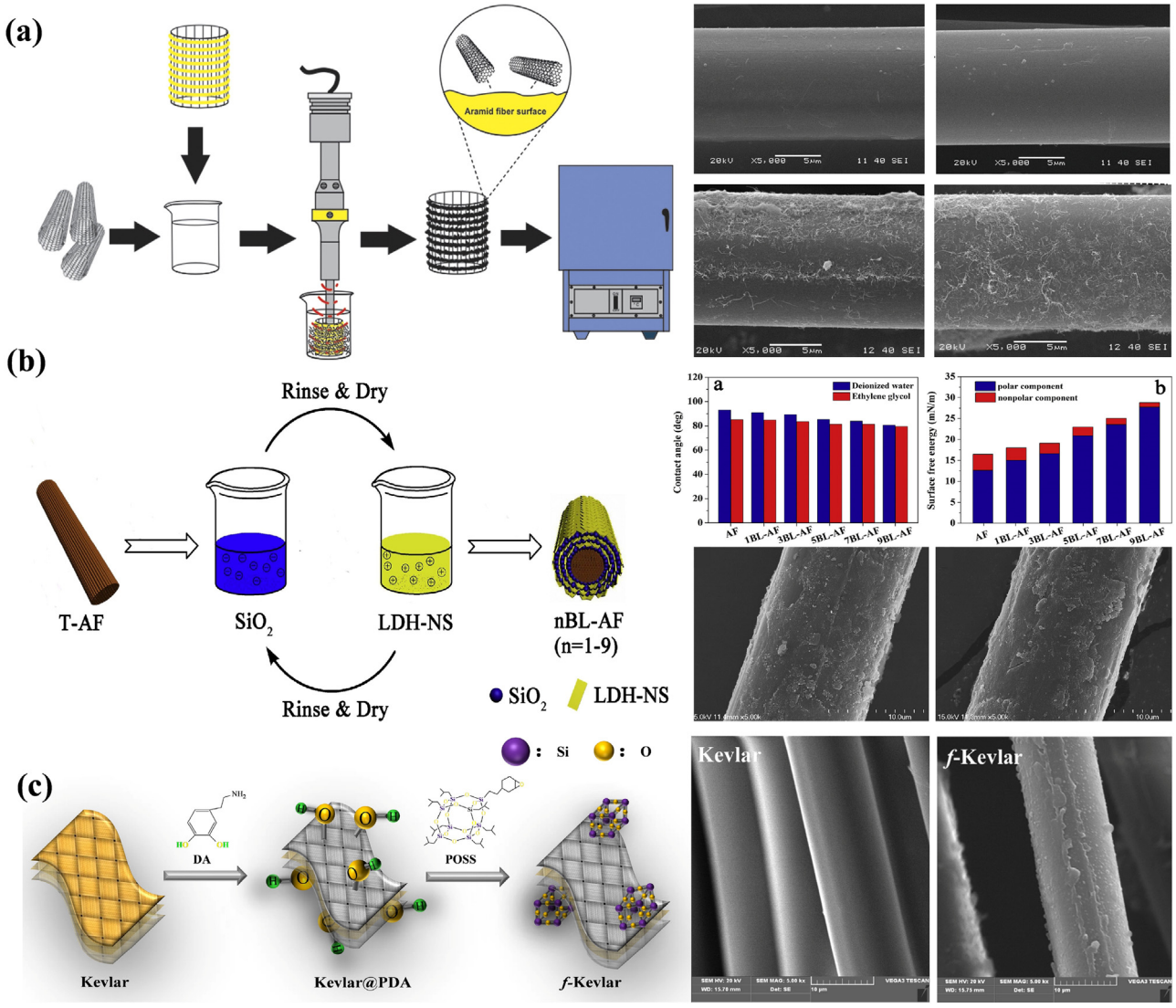

Fig. 11. Schematic diagram for deposition method of MWCNTs onto Kevlar fibers (a). Reprinted with permission from Ref. [196]. Copyright (2016) Elsevier B.V. Schematic diagram for preparation of Kevlar fibers through LBL self-assembly process (b). Reprinted with permission from Ref. [197]. Copyright (2017) Elsevier B.V. Schematic diagram for combining method of dopamine/POSS (DA/POSS) to functionalize the surface of Kevlar (*f*-Kevlar) fibers (c). Reprinted with permission from Ref. [200]. Copyright (2019) Elsevier Ltd.

face. The interfacial shear strength (IFSS) of TA coated UHMWPE fibers/epoxy composites increased by 43.3 %, compared with that of pure UHMWPE fibers/epoxy composites (Fig. 12(a)). Jin et al. [205] applied oxygen plasma to pretreat UHMWPE fibers, then coated polypyrrole (PPy) on their surfaces. The functionalized UHMWPE fibers present better interfacial bonding strength with epoxy resin due to the hydrogen bonding. And the single fiber pull-out strength of the functionalized UHMWPE fibers/epoxy resin micro-composites increased from 1.05 MPa (pure UHMWPE fibers/epoxy resin) to 10.05 MPa. Shanmugam et al. [206] adopted DA to coat UHMWPE (UHMWPE-PDA) fibers. Compared with pure UHMWPE fibers/thermoplastic (Elium®) resin composites, the ILSS of UHMWPE-PDA fibers/thermoplastic (Elium®) resin composites increased by 25.1 %. Ahmadi et al. [207] used dibenzoyl peroxide as the initiator and methyl glycidyl acrylate (GMA) as the monomer to initiate free radical polymerization and form poly(glycidyl methacrylate) on the surface of UHMWPE fibers, thereby containing a large amount of epoxy groups on the surface of UHMWPE fibers. The surface energy of the functionalized UHMWPE fibers increased from 33.39 mN/m (pure UHMWPE fibers) to 50.74 mN/m, and the corresponding contact angle decreased from 95.0° (pure UHMWPE fibers) to 87.7°. In addition, the ILSS of the functionalized UHMWPE fiber/epoxy composites increased from 2.44 MPa (pure UHMWPE fibers/epoxy resin) to 7.13 MPa.

5.2.3. *Poly(*p*-phenylene-2, 6-benzobisoxazole) (PBO) fibers*

The molecular chain of PBO fibers is composed of benzene ring and oxazole ring, and the angle between the external bonds of each ring is 180°, so that PBO fibers present a linear rigid rod-like molecular structure. Owing to their excellent comprehensive performance, PBO fibers have very broad application prospects in aerospace, weaponry, and other fields. The tensile strength of PBO fibers is 5.8 GPa, which is the highest among the known reinforced fibers. The initial decomposition temperature of PBO fibers is above 650 °C, and the long-term use temperature is 300 °C. Besides, PBO fibers present excellent chemical resistance, which is stable in most acid-based solutions, and only partially soluble in methanesulfonic acid (MSA) and polyphosphoric acid (PPA). In addition, PBO fibers possess high flame retardancy, low density, and low ϵ and tanδ, which is an ideal reinforced fibers for polymer matrix wave-transparent composites for radomes [208–210].

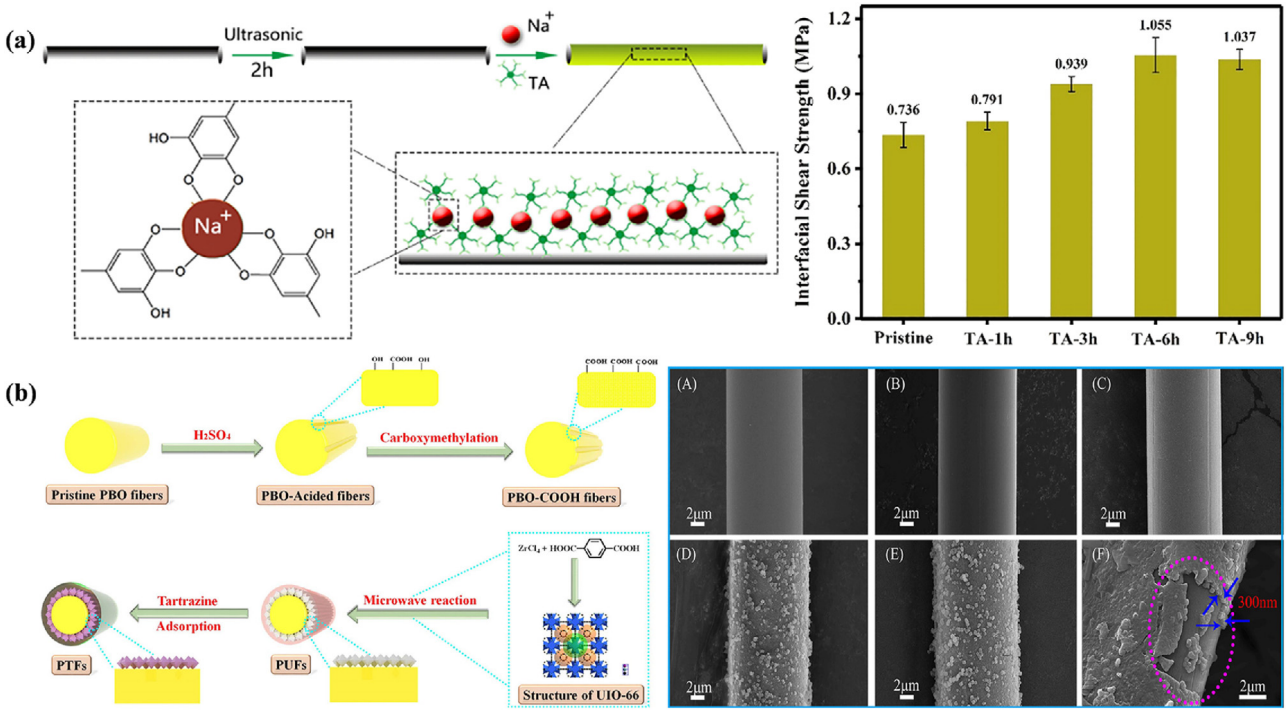

Fig. 12. Scheme diagram of surface functionalization of UHMWPE fibers with TA (a). Reprinted with permission from Ref. [204]. Copyright (2020) Society of Plastics Engineers. Schematic demonstration of the preparation process for PTFs (b). Reprinted with permission from Ref. [216]. Copyright (2018) American Chemical Society.

However, PBO fibers present smooth surface and extremely strong chemical inertness, resulting in poor interfacial compatibility with polymer matrix. Researchers usually apply acid, plasma, and high-energy radiation to functionalize the surface of PBO fibers. Wu et al. [211] used MSA to etch the surface of PBO fibers. The surface free energy of the functionalized PBO fibers was 46.2 mJ/m^2, increased by 34.4 %, compared with that of pure PBO fibers (62.1 mJ/m^2). And the ILSS (40.2 MPa) of the functionalized PBO fibers/epoxy composites increased by 15.8 %, compared with that of pure PBO fibers/epoxy composites (34.7 MPa). Liu et al. [212] adopted PPA/acetic acid to etch the surface of PBO fibers. The contact angle of functionalized PBO fibers with distilled water reduced from 90.0° (pure PBO fibers) to 42.8°. And the single fiber pull-out strength of the functionalized PBO fibers/epoxy resin micro-composites increased from 7.5 MPa (pure PBO fibers/epoxy resin) to 9.7 MPa. In our previous work [213], the high-modulus PBO (HMPBO) fibers were soaked in the solution of PPA and absolute ethanol (EtOH) (PPA: EtOH = 1:1, wt/wt), followed by ultrasonic treatment to prepare functionalized HMPBO fibers. The functionalized HMPBO fibers presented improved hydrophilicity, and the contact angle with distilled water reduced from 75.1° (pure HMPBO fibers) to 35.5°. Liu et al. [214] fabricated the functionalized PBO fibers treated by air plasma. When the intensity of the air plasma was 50 W/cm^3, the ILSS of the functionalized PBO fibers/BMI composites increased from 43.9 MPa (pure PBO fibers/BMI) to 57.1 MPa. However, the tensile strength of the functionalized PBO fibers decreased by 10.7 %, from 5.6 GPa (pure PBO fibers) to 5.0 GPa. Zhang et al. [215] grafted epichlorohydrin on the surface of PBO fibers through γ-ray radiation treatment. The functionalized PBO fibers possessed a large number of active groups and rough surfaces. When the intensity of γ-ray radiation is 30 kGy, the surface free energy of functionalized PBO fibers reached the maximum, increased by 14.5 %, compared with that of pure PBO fibers. The compound functionalization technique can exert the synergistic effect of the respective functionalization methods, in order to achieve the effect of 1 + 1 > 2. Hu et al. [216] adopted acid treatment and chemical grafting to functionalize the surface of PBO fibers. Firstly, PBO fibers was treated by H_2SO_4 to obtain PBO—COOH fibers, which was then grafted by metal-organic framework (MOF, UIO-66) and tartrazine to prepare PBO@Tartrazine fibers (PTFs) (Fig. 12(b)). Compared with that of pure PBO fibers, the single fiber pull-out strength of PTFs/epoxy resin micro-composites increased by 49.0 %. In our previous work [217], oxygen plasma and POSS were combined to functionalize the surface of HMPBO fibers. Compared with that of pure HMPBO fibers/CE micro-composites, the single fiber pull-out strength of functionalized HMPBO fibers/CE micro-composites increased by 20.7 %. The above methods can effectively improve the surface activity of PBO fibers to a certain extent, but also inevitably damage the intrinsic mechanical properties of PBO fibers.

Surface coating has attracted the attention of researchers as it does not damage the intrinsic structure of PBO fibers. Qian et al. [218] employed nano-titania (TiO_2) to coat the PBO fibers. The functionalized PBO fibers presented excellent interfacial bonding strength with epoxy resin. And the single fiber pull-out strength of the functionalized PBO fibers/epoxy resin micro-composites increased from 13.5 MPa (pure PBO fibers/epoxy resin) to 17.4 MPa. Zhu et al. [219] built a polyetherimide (PEI)/TiO_2 organic-inorganic hybrid coating on the surface of PBO fibers, which significantly improved their surface roughness. Yu et al. [220] designed and fabricated graphene oxide-metal organic framework (RGO-UIO-66) hybrid coating which was then coated on the surface of PBO fibers (PGU-CHF). The ILSS of PGU-CHF fibers/thermoplastic polyurethane composites increased from 63.2 MPa (pure PBO fibers/thermoplastic polyurethane) to 71.3 MPa. Meanwhile, PGU-CHF fibers also possessed excellent UV resistance. Lysozyme can rapidly self-assemble at a gas-liquid or liquid-solid interface under certain environmental conditions to form insoluble aggregates or two-dimensional nano-films with ordered structure, which can quickly, gently, and stably adhere to various materials surface. In our previous work [221], lysozyme was coated on the surface of PBO fibers (PBO@lysozyme), which was then grafted with epoxy-based

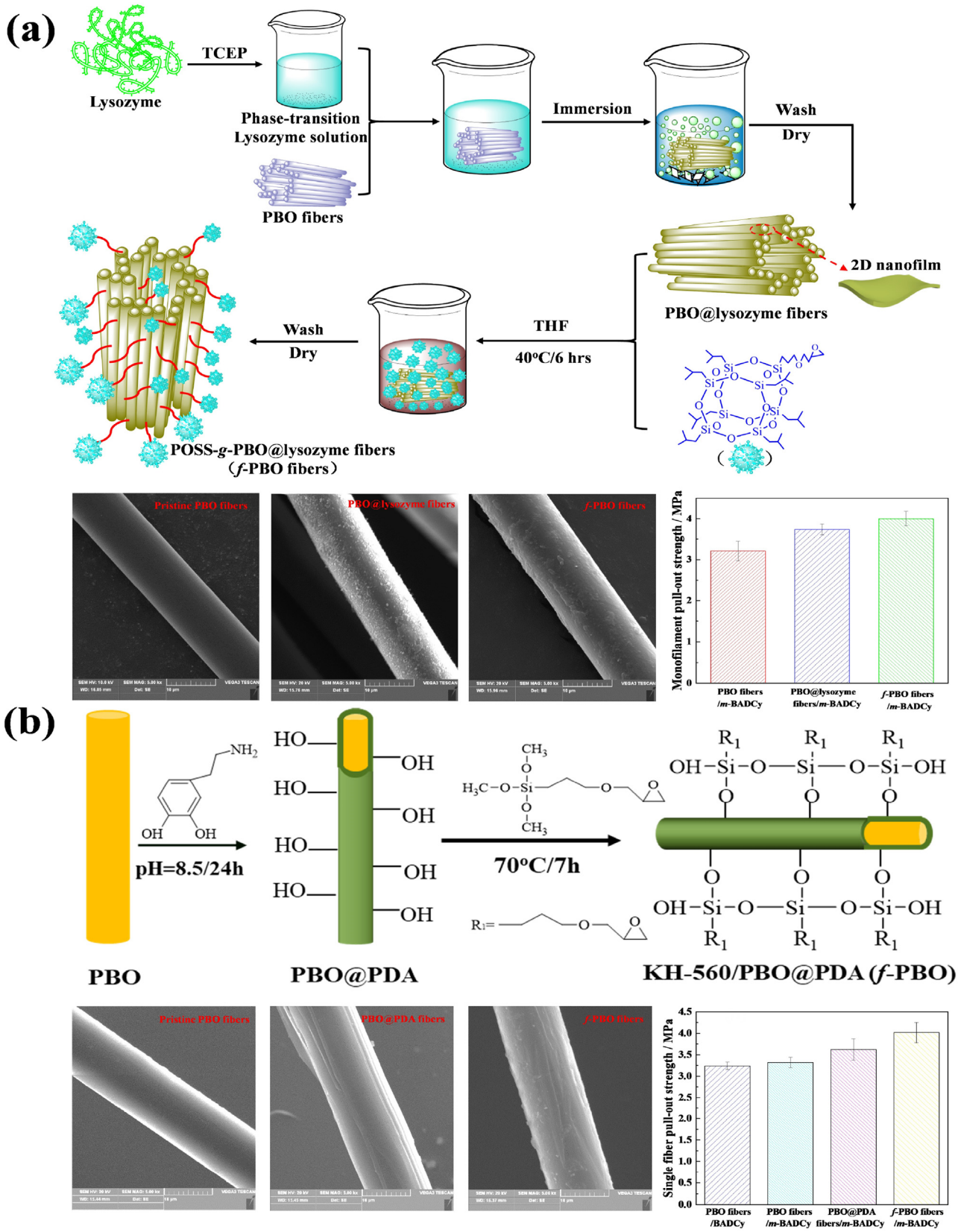

Fig. 13. Schematic diagram of the fabrication process of functionalized PBO (*f*-PBO) fibers lysozyme and epoxy-based POSS (a). Reprinted with permission from Ref. [221]. Copyright (2018) The Royal Society of Chemistry. Schematic diagram of PDA/KH-560 functionalized PBO fibers (b). Reprinted with permission from Ref. [223]. Copyright (2018) Elsevier Ltd.

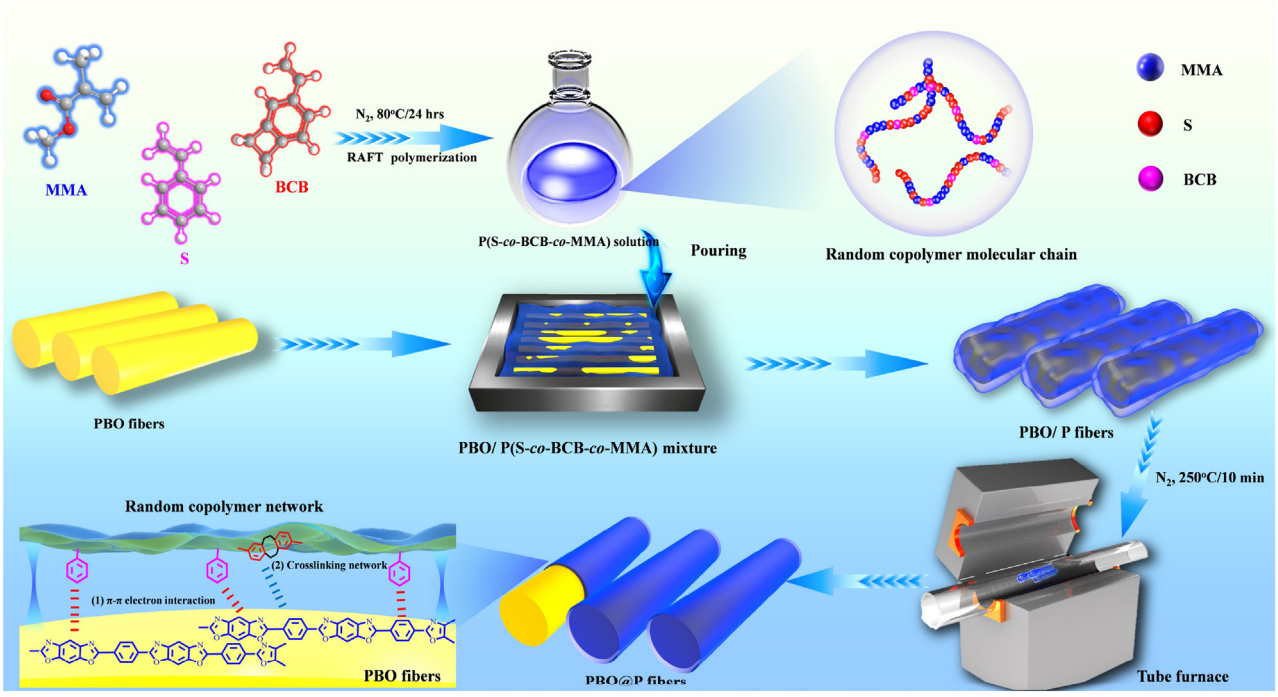

Fig. 14. Schematic diagram of functionalization of PBO fibers by coating random copolymer membrane. Reprinted with permission from Ref. [224]. Copyright (2020) Elsevier Ltd.

POSS to prepare functionalized PBO fibers (*f*-PBO). The ILSS of the *f*-PBO fibers/*m*-BADCy composites increased from 38.7 MPa (pure PBO fibers/*m*-BADCy) to 47.6 MPa, increased by 23.0 % (Fig. 13(a)). In addition, DA is also used to functionalize the surface of PBO fibers. Chen et al. [222] adopted branched polyethyleneimine (b-PEI)/graphene oxide/PDA to functionalize the surface of PBO fibers (PBO@PDA-PEI-GO). The surface roughness of PBO@ PDA-PEI-GO fibers increased from 26.6 nm (pure PBO fibers) to 69.4 nm, and the single fiber pull-out strength of PBO@PDA-PEI-GO fibers/epoxy micro-composites was 68.2 MPa, 68.8 % higher than that of PBO fibers/epoxy resin micro-composites (40.4 MPa). In our previous work [223], DA and KH-560 were synchronously performed to functionalize the surface of PBO fibers (*f*-PBO). Compared with that of pure PBO fibers, the interfacial bonding strength between *f*-PBO fibers and modified CE resin increased by 25 % (Fig. 13(b)). Moreover, Gu et al. [224] synthesized random copolymers (P(S-*co*-BCB-*co*-MMA)) containing benzocyclobutene in the side-chain by reversible addition-fragmentation chain transfer (RAFT) polymerization, which were then utilized to form dense random copolymer membrane on the surface of PBO fibers by thermally cross-linking (PBO@P fibers, Fig. 14). When the *M*n of P(S-*co*-BCB-*co*-MMA) was 32300, the surface roughness of PBO@P fibers was increased from 11 nm (PBO fibers) to 39 nm. In addition, PBO@P fibers presented the optimal interfacial compatibility with BADCy resins. And the single fiber pull-out strength of PBO@P fibers/BADCy micro-composites was 4.5 MPa, increased by 45.2 % in comparison with that of PBO fibers/BADCy micro-composites (3.1 MPa).

Recent years, designing and synthesizing interfacial compatibilizers, which present excellent compatibility with PBO fibers and polymer matrix to improve the ILSS of polymer matrix wave-transparent composites (PBO fibers/polymer matrix) without damaging the intrinsic structure of PBO fibers, have attracted wide attention of researchers. Liu et al. [225] designed and prepared a novel interfacial compatibilizer (PCOO) based on hydroxyphosphorated castor oil and epoxy resin to functionalize the PBO fibers. The single fiber pull-out strength of PBO fibers/PCOO/epoxy resin micro-composites increased by 156.2 % in comparison with that of pure PBO fibers/epoxy resin micro-composites. In our previous work [226], a novel interfacial compatibilizer of epoxy-terminated poly (p-phenylene-2, 6-benzobisoxazole) precursor (epoxy-prePBO) was synthesized to modify BADCy resin *via* copolymerization. When the amount of epoxy-prePBO was 7 wt%, the PBO-*co*-BADCy resin presented the best interfacial bonding strength with PBO fibers. The ILSS of PBO fibers/PBO-*co*-BADCy resin composites increased by 20.1 % in comparison with that of pure PBO fibers/BADCy resin composites.

6. Test methods for dielectric properties

Dielectric properties (ϵ and tanδ) are the main indicators for evaluating the wave transmission performance of polymer matrix wave-transparent composites. At present, test methods for dielectric properties mainly include resonance methods, transmission line methods and free space methods [227–229].

6.1. Resonance methods

Resonance methods are to calculate the complex dielectric constant of polymer matrix wave-transparent composites by measuring the resonance frequency (f) and quality factor (Q) before and after loading the samples in the cavity. It mainly includes perturbation method, high-Q cavity method, and quasi-optical cavity method [230–232].

6.1.1. Perturbation method

The perturbation method obtains the ϵ and tanδ of the samples by comparing the changes of the electromagnetic field structure and resonance parameters in the cavity with or without samples [233–235]. The testing device for perturbation method generally includes the rectangular perturbation cavity and cylindrical perturbation cavity, as shown in Fig. 15.

The vector network analyzer is used to measure the f and Q values of the cavity before and after the disturbance. And the dielectric

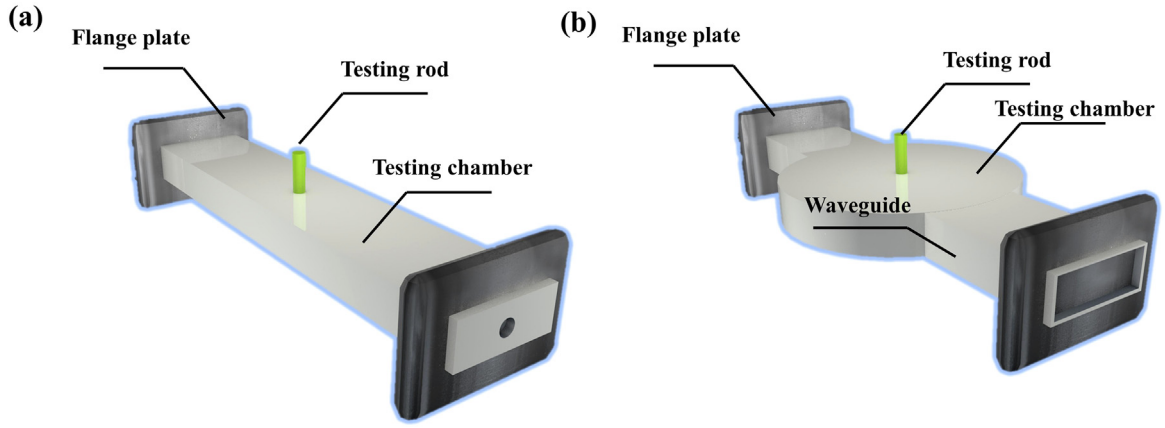

Fig. 15. Schematic diagram of testing device for perturbation methods: rectangular perturbation cavity (a); cylindrical perturbation cavity (b).

properties of the samples are calculated according to the perturbation theory. The ϵ can be calculated by the following formula:

Round bar samples

$$\epsilon' = 1+2K\left[\frac{aL}{\pi d_s^2}\right]\left[\frac{f_{00}-f_{00}}{f_{0s}}\right] \tag{7}$$

Rectangular bar samples

$$\epsilon' = 1+\frac{1}{2}K\left[\frac{aL}{\pi Wt}\right]\left[\frac{f_{00}-f_{00}}{f_{0s}}\right] \tag{8}$$

where, f_{00} represents the cavity resonance frequency; f_{0s} represents the resonance frequency of the test cavity with samples; d_s represents the diameter of the round bar sample; a represents the width of the rectangular cavity; L represents the length of the rectangular cavity; W represents the width of rectangular bar samples; t represents the thickness of the rectangular bar samples; K represents the correction factor of the perturbation formula. The tanδ can be calculated by the following formula:

Round bar samples

$$\tan\delta = \frac{aL}{\pi\epsilon' d_s^2}\left[\frac{1}{Q_{0s}}-\frac{1}{Q_{00}}\right] \tag{9}$$

Rectangular bar samples

$$\tan\delta = \frac{aL}{4\epsilon' Wt}\left[\frac{1}{Q_{0s}}-\frac{1}{Q_{00}}\right] \tag{10}$$

where, Q_{00} represents the unloaded quality factor of the test cavity; Q_{0s} represents the unloaded quality factor of the test cavity with samples.

The perturbation method is based on dielectric perturbation theory, which is suitable for testing low-loss materials. However, the disturbance of the high-loss materials is too large, which greatly reduces the accuracy of the above perturbation method.

6.1.2. High-Q cavity method

High-Q cavity method is divided into two categories. One is to fix f and change the cavity size (fixed frequency method), the other is to fix the cavity size and change f (frequency conversion method) [236,237]. The samples tested by high-Q cavity method are in a non-contact state with the cavity wall, and generally does not require gap correction. Therefore, the high-Q cavity method has a high-test accuracy for low-loss samples (shown in Fig. 16). In principle, the high-Q cavity method presents no special restrictions on the test frequency, but the lower the test frequency, the larger the volume of the high-Q resonator system and samples size required, thereby increasing the difficulty of preparing the samples. After inserting the samples at the bottom of the high-Q cavity, the ϵ_0 of the samples is different from the ϵ_0 of air, which causes the equivalent axial distance of the cylindrical resonant cavity to change, resulting in a change in f. And the Q value of the cylindrical resonator decreases with the increase of tanδ, so the ϵ and tanδ of the samples can be calculated according to the f and Q of the cylindrical resonator with and without samples.

The derivation process of ϵ is as follows:

For **system 1**:

$$(f_0 D)^2 = \left(\frac{c}{\pi}X_{01}\right)^2 + \left(\frac{cn}{2}\right)^2\left(\frac{D}{L}\right)^2 \tag{11}$$

For **system 2**:

$$\beta_\epsilon^2 = \left(\frac{2\pi f_0\epsilon}{c}\right)\epsilon' - \left(\frac{2X_{01}}{D}\right)^2 \tag{12}$$

$$\beta_0^2 = \left(\frac{2\pi f_0\epsilon}{c}\right) - \left(\frac{2X_{01}}{D}\right)^2 \tag{13}$$

$$\frac{\tan\beta_\epsilon d}{\beta_\epsilon} - \frac{\tan\beta_0(1-d)}{\beta_0} = 0 \tag{14}$$

where, X_{01} represents the root of the Bessel function, β_0 and β_ϵ represent the propagation constants of the air part and the loaded medium part of the cylindrical resonator, respectively. And D, n, X_{01}, and the speed of light (c) are known. L can be obtained by measuring f_0, β_0 can be obtained by measuring $f_{0\epsilon}$, and β_ϵ can be obtained by Eqs. (13) and (14), ϵ' can then be calculated accordingly.

According to the relationship between energy storage and energy consumption of **System 2**, the Eq. (15) can be obtained:

$$\tan\delta = \left(1+\frac{u}{p\nu\epsilon'}\right)\cdot\left(\frac{1}{Q_{0\epsilon}}-\frac{1}{Q_{00}}\right) \tag{15}$$

where:

$$\frac{1}{Q_{00}^1} = \frac{1}{Q}\left(\frac{f_0}{f_{0\epsilon}}\right)^{\frac{5}{2}}\cdot\frac{\left(\frac{2X_{01}}{D}\right)^2\cdot(p\nu+u)+D\left(p\beta_\epsilon^2+\beta_0^2\right)}{(p\nu\epsilon'+u)\cdot\left[\left(\frac{2X_{01}}{D}\right)^2\cdot\left(1-\frac{D}{L}\right)+\left(\frac{2\pi f_0}{c}\right)^2\cdot\frac{D}{L}\right]} \tag{16}$$

$$p = \left[\frac{\sin\beta_0(L-d)}{\sin\beta_0 d}\right]^2 \tag{17}$$

$$u = 2(L-d)-\frac{\sin 2\beta_0(L-d)}{\beta_\epsilon} \tag{18}$$

$$\nu = 2d-\frac{\sin 2\beta_0 d}{\beta_\epsilon} \tag{19}$$

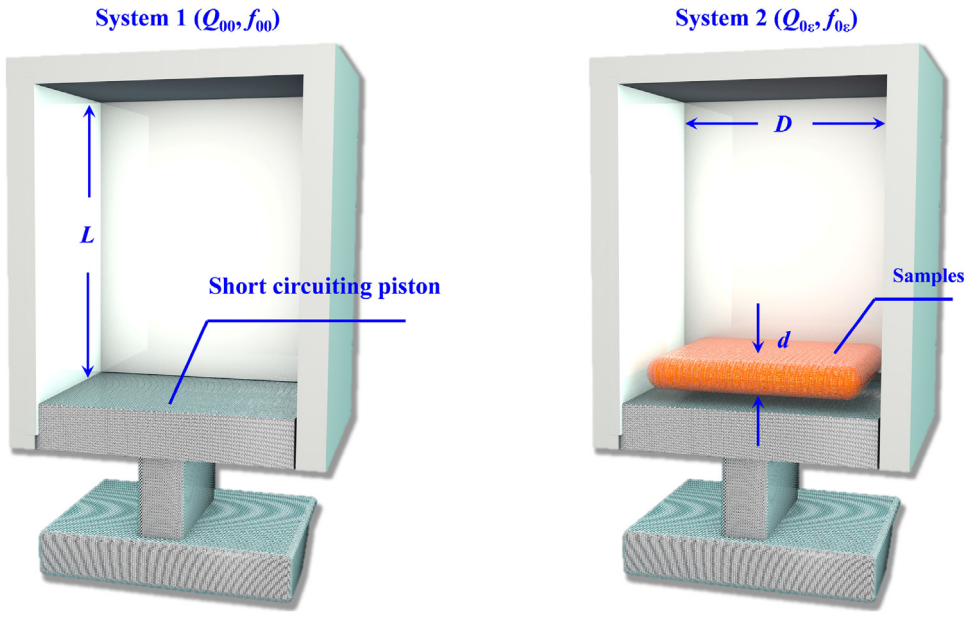

Fig. 16. Schematic diagram of testing principle for high Q cavity method.

Therefore, tanδ can be obtained by subjecting the quality factor (Q_{00}) of the cavity and the unloaded quality factor ($Q_{0\epsilon}$) of the cavity.

6.1.3. Quasi-optical cavity method

Quasi-optical resonant cavity is developed from the optical Fabry-Perot interferometer [238,239]. The commonly used quasi-optical cavity mainly include two types. The first type of the reflection mirror is composed of two spherical mirrors, and the samples are loaded in the middle. The second type of the reflection mirror is composed of a plane mirror and a spherical mirror, and the samples are loaded on the plane mirror position (as shown in Fig. 17). R represents the radius of the spherical mirror, D represents the distance between the two mirrors (also known as the cavity length), and the part between the two dashed lines is the beam range in the cavity.

The basic principle of the quasi-optical cavity method is to calculate the ϵ and tanδ by comparing the changes of f, cavity length, and Q with or without samples, and combining the thickness of samples and the initial length of cavity. Compared with closed resonators such as perturbation method and high-Q cavity method, the quasi-optical cavity method presents many advantages such as openness, higher Q value, simple working mode, sparse mode, and accuracy. Therefore, the quasi-optical cavity method is suitable for testing high-frequency dielectric properties, such as millimeter waves, sub-millimeter waves, and terahertz, *etc.*

The accuracy and f of the quasi-optical cavity method are closely related to the thickness of samples. Choosing appropriate f and samples' thickness can obtain a sufficiently high-precision measurement. Therefore, it is necessary to predict the ϵ and tanδ before the measurement and design an appropriate samples' thickness, so as to obtain accurate results of the dielectric properties.

The ϵ can be obtained from the electric field equation [236]:

$$\tan[n\epsilon t - \phi(t)] = n\tan[-\epsilon d - \phi_2(t) + \phi_2(t+d)] \tag{20}$$

where, n represents the refractive index of the medium; t represents the thickness of the medium; d is the difference between the distance of the two mirrors and the thickness of the medium. Taking ϕ_T=$\phi_1(t)$ and ϕ_D=$\phi_2(t + d)$-$\phi_2(t)$, the ϵ_r of the samples can be calculated from the following equations:

$$\frac{1}{n}\tan[n\epsilon t - \phi_T] = -\tan[\epsilon d - \phi_D] \tag{21}$$

$$\phi_T = \arctan(\frac{t}{ns_0}) \tag{22}$$

$$\phi_D = \arctan(\frac{d'}{s_0}) - \arctan(\frac{t}{ns_0}) \tag{23}$$

$$w_0^2 = \frac{2}{k}\sqrt{(d+\frac{t}{n^2})\cdot(R_0 - d - \frac{t}{n})} \tag{24}$$

$$s_0 = \sqrt{d'(R_0 - d')} \tag{25}$$

$$d = D - t \tag{26}$$

$$d' = d + \frac{t}{n} \tag{27}$$

$$n = \sqrt{\epsilon_r} \tag{28}$$

The corresponding ϵ_r values of the samples can be calculated by subjecting the obtained t and resonance parameters values into the above equations.

In addition, tanδ can be calculated from the following equations:

$$\tan\delta = \frac{1}{Q_e}\cdot\frac{t\Delta - d}{t\Delta + \sin[2(\epsilon d - \phi d)]} \tag{29}$$

$$\frac{1}{Q_e} = \frac{1}{Q_{0s}} - \frac{1}{Q_1} \tag{30}$$

$$\frac{1}{Q_1} = Q_{00}\cdot\frac{2(t\Delta+\mathrm{d})}{D(\Delta+1)} \tag{31}$$

$$\Delta = \frac{n^2}{n^2\cos^2(n\epsilon t - \phi_t) + \sin^2(n\epsilon t - \phi_t)} \tag{32}$$

where, Q_{0s} represents the unloaded quality factor with samples; Q_1 represents the unloaded quality factor with ideal lossless sample; Q_{00} represents the inherent quality factor of the resonant cavity.

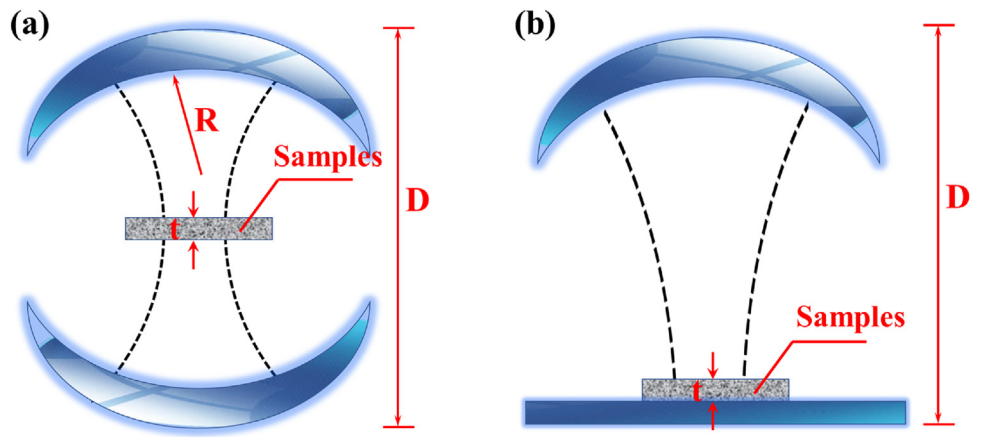

Fig. 17. Schematic diagram of testing principle for quasi-optical cavity method: symmetrical structure (a) and hemihedrism structure (b).

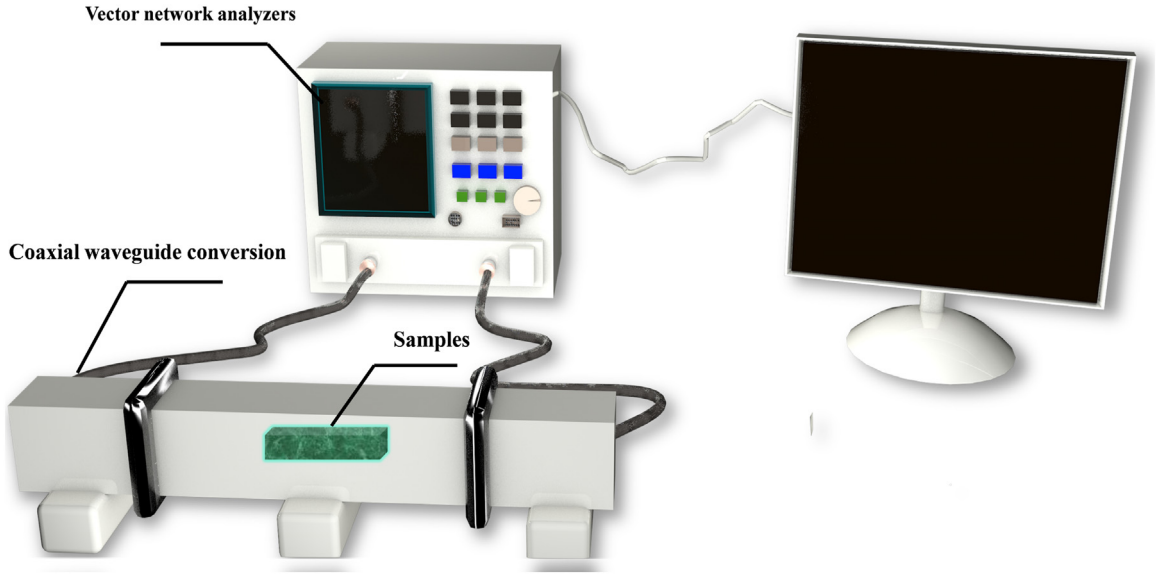

Fig. 18. Schematic diagram for the measurement of dielectric properties with waveguide transmission method.

6.2. Transmission line method

The principle of transmission line method is to measure the transmission parameter of the transmission line, and the complex dielectric constant (ϵ_r^*) of the samples can be calculated according to the amplitude and phase position. This method is suitable for liquids or high-loss medium and presents simple measurement process and high accuracy [240–242]. At present, the transmission lines mainly include coaxial lines, waveguides (Fig. 18) and other types of transmission lines [243].

Assuming that the single master model of wave transmission is the transverse electric (TE) mode, the characteristic impedance is Z_0, the operating wavelength is λ, the wavelength of waveguide is λ_g, and the cut-off wavelength is λ_c, when the samples are placed in the waveguide, the characteristic impedance (Z_ϵ) of the samples waveguide can be calculated as follows [244]:

$$Z_\epsilon = \frac{120\pi}{\sqrt{\epsilon_r u_r - \left(\frac{\lambda}{\lambda_c}\right)^2}} \tag{33}$$

For polymer matrix wave-transparent composites and other electrically nonconducting materials, the u_r is equal to 1, then:

$$Z_\epsilon = \frac{120\pi}{\sqrt{\epsilon_r - \left(\frac{\lambda}{\lambda_c}\right)^2}} \tag{34}$$

The device is filled with air before measurement, so the ϵ_r is equal to 1, then:

$$Z_0 = \frac{120\pi}{\sqrt{1 - \left(\frac{\lambda}{\lambda_c}\right)^2}} \tag{35}$$

Taking $C_\epsilon = (Z_0/Z_\epsilon)^2$, Eq. (36) can be obtained from Eqs. (34) and (35):

$$C_\epsilon = \frac{\epsilon_r - \left(\frac{\lambda}{\lambda_c}\right)^2}{1 - \left(\frac{\lambda}{\lambda_c}\right)^2} \tag{36}$$

Considering $1/\lambda^2 = 1/\lambda_c{}^2 + 1/\lambda_g{}^2$, Eq. (36) can be changed to:

$$\epsilon_r = \frac{C_\epsilon + \left(\frac{\lambda_g}{\lambda_c}\right)^2}{1 + \left(\frac{\lambda_g}{\lambda_c}\right)^2} \tag{37}$$

When C_ϵ is a complex number, making $C_\epsilon = A_\epsilon + jB_\epsilon$, the $\epsilon_r{}^*$ is expressed as Eq. (38):

$$\epsilon_r^* = \epsilon_r^{'} - j\epsilon_r^{''} = \frac{A_\epsilon + jB_\epsilon + \left(\frac{\lambda_g}{\lambda_c}\right)^2}{1 + \left(\frac{\lambda_g}{\lambda_c}\right)^2} \tag{38}$$

The real and imaginary parts of $\epsilon_r{}^*$ are expressed as follows:

$$\epsilon_r^{'} = \frac{A_\epsilon + \left(\frac{\lambda_g}{\lambda_c}\right)^2}{1 + \left(\frac{\lambda_g}{\lambda_c}\right)^2} \tag{39}$$

$$\epsilon_r^{''} = \frac{-B_\epsilon}{1 + \left(\frac{\lambda_g}{\lambda_c}\right)^2} \tag{40}$$

Based on the above equations, the $\epsilon_r{}^*$ can be calculated after measuring the propagation parameters.

6.3. Free space method

The free space method is a non-resonant method without damaging the samples. It can perform wide-band sweep and orientation tests for the samples. In addition, this method is applicable in a wide temperature range. It has no special requirements for the shape of the samples [245]. However, the surface area of the samples needs to be large enough to ensure reception and propagation of signals. The free space method is widely used in the field of microwave remote sensing to measure the ϵ of samples with large surface area [246]. The schematic diagram of measurement by free space method is shown in Fig. 19.

When the wavelength of the electromagnetic wave is much greater than the surface roughness of the samples, the relationship between the ϵ_r of the samples and the measurement angles can be described by the Fresnel Reflection Coefficient (Eqs. (40) and (41)):

$$R_H = \frac{\cos\theta - \sqrt{\epsilon_r - \sin^2\theta}}{\cos\theta + \sqrt{\epsilon_r - \sin^2\theta}} \tag{40}$$

$$R_v = \frac{\epsilon_r \cos\theta - \sqrt{\epsilon_r - \sin^2\theta}}{\epsilon_r \cos\theta + \sqrt{\epsilon_r - \sin^2\theta}} \tag{41}$$

where, $\epsilon_r^* = \epsilon_r^{'} - j\epsilon_r^{''}$is the relative complex permittivity of the samples, θ represents the angle of incidence of the transmitting antenna, R_H represents the reflection coefficient of horizontal polarization, and R_v represents the vector reflection coefficient of vertical polarization. Provided $|-j\epsilon_r''/(\epsilon_r'-\sin^2\theta)|<1$, and making$P = \sqrt{\epsilon_r^{'} - \sin^2\theta}$, Eqs. (40) and (41) can be expressed as follows:

$$\left|R_H\right|^2 = \frac{\left(\cos\theta - p\right)^2 + \frac{\epsilon_r''^2}{4p^2}}{\left(\cos\theta + p\right)^2 + \frac{\epsilon_r''^2}{4p^2}} \tag{42}$$

$$\left|R_v\right|^2 = \frac{\left(\epsilon_r^{'}\cos - p\right)^2 + \epsilon_r''^2 \cdot \left(\frac{1}{2}p - \cos\theta\right)^2}{\left(\epsilon_r^{'}\cos + p\right)^2 + \epsilon_r''^2 \cdot \left(\frac{1}{2}p - \cos\theta\right)^2} \tag{43}$$

Based on the above equations, the $\epsilon_r{}^*$ of the samples is only related to the R_H, R_v, and θ. Therefore, the $\epsilon_r{}^*$ of the samples can be obtained after measuring the amplitude and phase position of the reflection parameters and system calibration (metal plate or relative calibration).

7. Applications of the polymer matrix wave-transparent composites

7.1. Aircraft radomes

Aircraft radomes mainly refer to the radomes for high Mach aircraft such as missiles, rockets, and satellites, which are an important part for aviation and aerospace weaponry [247]. In addition, aircraft radomes possess the advantages of high temperature, ablative & rain resistance, and excellent mechanical & electrical properties (low ϵ and tanδ) [248]. In 1950s, the Boeing Company of America adopted E-GFs to fabricate the "Pomac" radome for Mach 3 active guided missiles. In addition, the hypersonic missile radomes need to bear greater loads and thermal shocks in higher operating temperatures and in harsher environment, thereby placing higher requirements on the T and aiming error rate. China Aerospace Materials and Technology Research Institute developed quartz fiber fabrics wave-tranparent composites (low ϵ and tanδ), which were successfully applied to missile radomes. Georgia Institute of Technology in the United States designed and fabricated slurry-fused molten quartz fibers composites, which were used in the American "Patriot" air defense missile and the Italian Asped missile (Fig. 20). In addition, Russia focuses on the development of quartz fabrics reinforced radomes with stablility at 1500–1800 °C, which are widely used in cruise missiles, anti-missiles, tactical missiles, and space shuttles.

7.2. Radomes of ground, shipborne, and airborne

Aiming at ground radars with large-volume and high-power, ground radomes present wide-band wave-transparent performance, excellent electrical performance, high structural strength, anti-humidity performance, and good processability [249,250]. The main reinforced fibers and polymer matrix of the ground radomes are glass fibers and UP resin, respectively. For example, D331 5 G base station radome (Fig. 21(a)) fabricated by Dongguan MIYABI-FRP Limited and 140 communication radar radome (Fig. 21(a')) fabricated by Harbin Topfrp Composite Ltd. Co. have been widely applied in the market. In addition, the ground radomes developed by Jinfa Technology Corporation, Lotte Korea, and DuPon have been widely used in ground base stations and other fields.

With the upgrading of shipborne radar antenna systems, the shipborne radomes are required to possess multiple functions such as rectification, bearing, wave-transparent, and environmental adaptability [251,252]. The reinforced fibers are mainly quartz fibers. CE resins, silicone resins, and PTFE resins are often used as polymer matrix. For example, "Xue Long" shipborne radome designed by Laoling Jingbei Rongye composite material Co., Ltd (Fig. 21(b)) and the type 120 shipborne radome (Fig. 21(b')) fabricated by Harbin Topfrp Composite Co., Ltd. have been widely used in shipborne radomes and other fields.

As an aerodynamic/structure/wave-transparent integrated functional composites, airborne radomes not only prevent radar antennas from the invasion of heavy rain, strong wind, ice, snow, sand, solar radiation, and salt fog, but also are the window of receiving and transmitting electromagnetic wave [7,253]. Meanwhile, the airborne radome, as an integral part of the aircraft, also plays a role in maintaining the overall aerodynamic shape of the aircraft [254]. At present, quartz fibers and Kevlar fibers are common reinforced fibers for airborne radomes. For example, the tapered radome of the US F-15 and F-22 fighters adopted quartz fibers/CE resin composites with excellent broadband performance. In addition, the paddle-shaped airborne radome fabricated by US Gunsner Aircraft Company and the challenger airborne radome fabricated

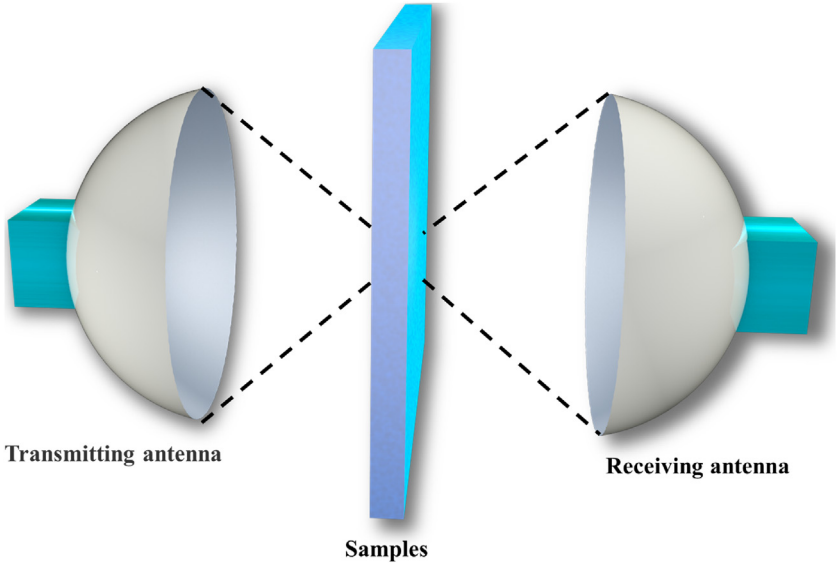

Fig. 19. Schematic diagram of measurement by free space method.

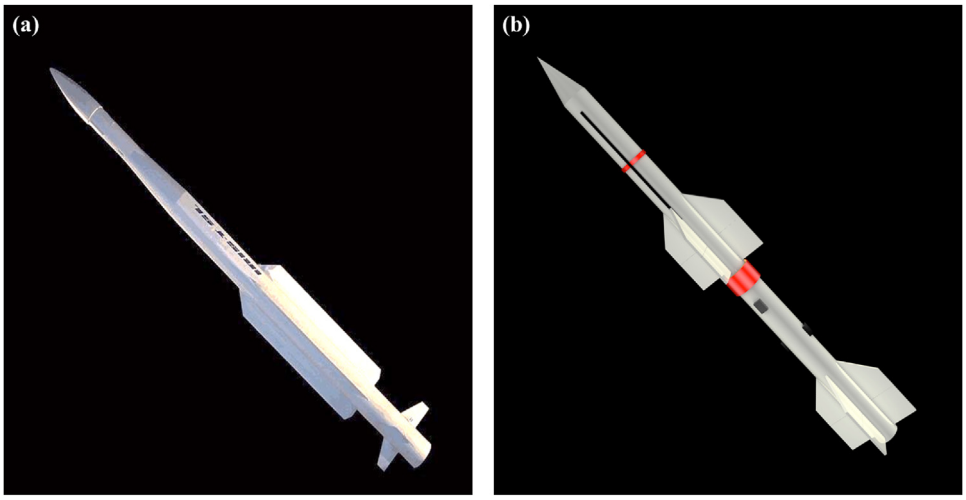

Fig. 20. Patriot air defense missile (PAC-3) (a) and Aspie air-to-air missile (b).

by Canadian Aircraft Manufacturing Company both adopted Kevlar fibers-reinforced wave-transparent composites.

7.3. Print circuit board

Print circuit board (PCB), as the support part and the carrier for transmitting signals of electronic components (Fig. 22), has been widely used in the fields of aerospace, medical equipments, communication services, computers, and civil industries due to excellent mechanical properties and high wave transmission performance (low ϵ and tanδ, enabling high-speed and high-fidelity transmission of signals) [255,256]. At present, the GFs/FR-4 epoxy composites fabricated by the National Electronics Manufacturers Association (NEMA) are used as the standard for PCB in industrial field. In the 1960s, the GFs/epoxy composites had been used as PCB for industrial and civilian electronic equipments in Japan. In addition, Qisheng and Daikin Industrial Corporation in Japan, TTM Technology Corporation in the United States, and Kingboard Group Corporation in China adopted CE resins to prepare PCB. With the advent of the 5 G technology, the performance and operating speed of electronic devices will be greatly improved, which puts higher requirements on the performances of PCB [257]. Zigong Tianlong Chemical Corporation and Nanya Circuit Board Corporation have developed a series of fluorine-based resin substrates such as PTFE and fluorine-containing PI resin, which are widely applied in the field of PCB with high integration, high speed, and high frequency.

8. Conclusions and outlook

Polymer matrix wave-transparent composites play an extremely important role in cutting-edge industries such as aerospace, transportation, and 5 G communication services. This review focuses on the latest research progress and achievements of polymer matrix wave-transparent composites from the types of polymer matrix, reinforced fibers, and surface functionalization. The dielectric properties and heat resistance of the polymer matrix play a leading role in the T and service temperatures. The mechanical properties, wave transmission performance, and heat-resistant properties of the reinforced fibers determine the overall mechanical properties of polymer matrix wave-transparent composites, and also affect the T and service temperature. Meanwhile, the interface between reinforced fibers and polymer matrix is the

Fig. 21. D331 5 G base station radome (a), and 140 ground communication radome (a'); "Xue Long" shipboard radome (b), and 120 shipboard radome (b').

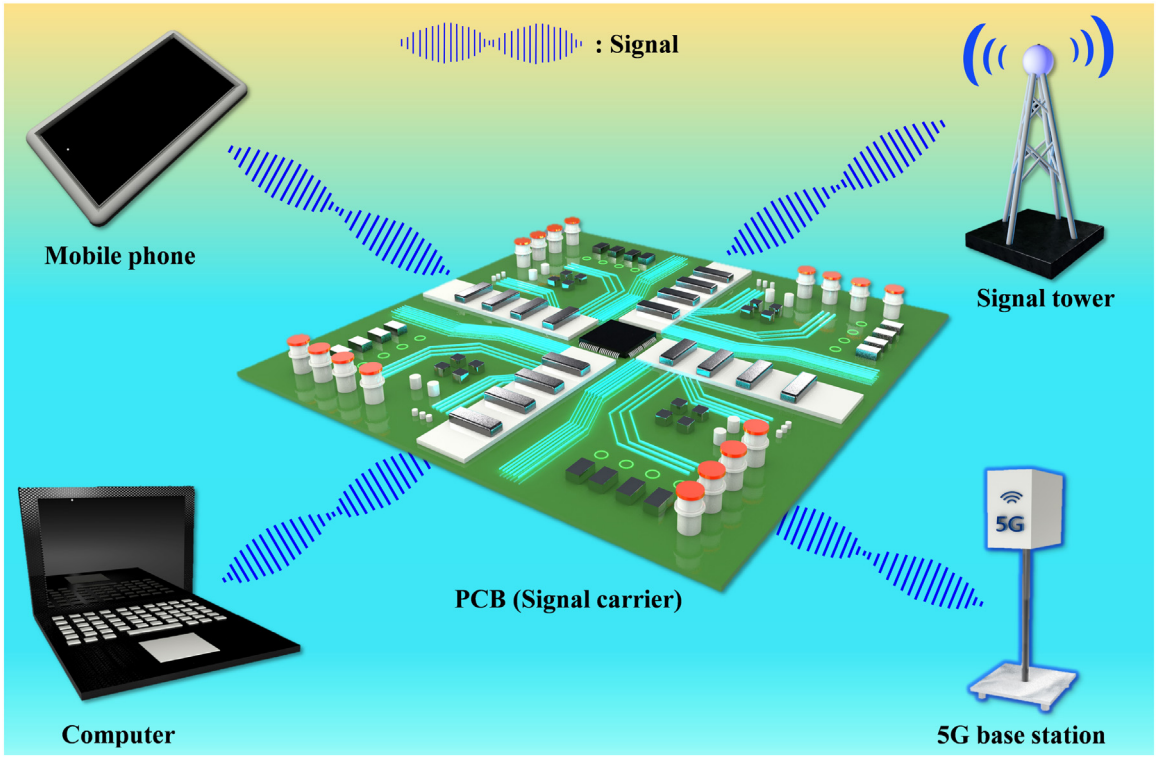

Fig. 22. Schematic diagram of signal transmission for PCB in electronic equipments.

main obstacle affecting the wave transmission performance and mechanical properties of the polymer matrix wave-transparent composites.

However, there are still three key scientific and technical problems to be solved urgently in the research filed of the polymer matrix wave-transparent composites. (1) How to efficiently

improve the surface activity of reinforced fibers (especially PBO fibers) without destroying their intrinsic structures, finally to truly achieve their excellent interfacial bonding strength with polymer matrix; (2) How to realize the synergistic improvement of the dielectric properties (wave transmission performance), mechanical properties, and high-temperature resistance through integrated structure/function design, to meet the high requirements of the new generation radomes; (3) How to establish several more accurate wave-transparent models to explain the internal relationship of "molecular chain-electromagnetic wave-wave transmission properties", and develop the wave transmission mechanism.

Based on the research status and development trend of polymer matrix wave-transparent composites, the following related studies require urgent attention. (1) Making full use of mathematics and computer science to establish wave-transparent models, adopting simulation software to dynamically simulate the reflection, loss, and transmission process of electromagnetic wave, and finally to illustrate the transmission mechanism. (2) Developing efficient surface functionalization methods of reinforced fibers, analyzing & characterizing the surface pefotmances of reinforced fibers and the transmission process of electromagnetic wave at the interface applying advanced testing technology, in order to reveal the nature of interfacial compatibility and interfacial polarization from a microscopic perspective. (3) Designing and synthesizing novel high-performance polymer matrix with high temperature resistance, low ϵ and tanδ, and studying the internal effects and potential mechanism of the short-range, long-range, and aggregate state structures on the intrinsic ϵ and tanδ of the polymer matrix. (4) Carrying out researches on the practical engineering and related basic science problems, to accelerate the upgrading and application of the polymer matrix wave-transparent composites in aerospace, transportation, 5 G communication services, and other fields.

Declaration of Competing Interest

The authors report no declarations of interest.

Acknowledgements

The authors are grateful for the support and funding from National Scientific Research Project (Basis Strengthening Plan); Space Supporting Fund from China Aerospace Science and Industry Corporation (2020-HT-XG); Fundamental Research Funds for the Central Universities (310201911qd003); China Postdoctoral Science Foundation (2019M653735); State Key Laboratory for Modification of Chemical Fibers and Polymer Materials from Donghua University (KF2001); Open Fund from Henan University of Science and Technology (2020-RSC02); This work is also financially supported by Polymer Electromagnetic Functional Materials Innovation Team of Shaanxi Sanqin Scholars.

References

[1] L. Su, M. Li, H. Wang, M. Niu, D. Lu, Z. Cai, ACS Appl. Mater. Inter. 11 (2019) 15795–15803.
[2] X.W. Yin, L.F. Cheng, L.T. Zhang, N. Travitzky, P. Greil, Int. Mater. Revi. 62 (2017) 117–172.
[3] Y. Zhao, Y. Zhang, H. Gong, H. Sun, Q. Li, Ceram. Int. 40 (2014) 13537–13541.
[4] Q. Qi, P. Zheng, Y. Lei, X. Liu,Compos. Part B-Eng. 173 (2019), 106915.
[5] T.J. Liu, M.C. Sil, C.M. Chen,Compos. Sci. Technol. 193 (2020), 108135.
[6] W. Su, N. Wu, B. Wang, H. Bao, Y. Wang, Mater. Lett. 216 (2018) 228–231.
[7] L. Zhou, Z. Liu, L. Tang, Y. Pei, Mater. Des. 114 (2017) 264–270.
[8] M.D. Huang, S.Y. Tan, Waves Random Complex 19 (2009) 409–417.
[9] X. Fan, J. He, J. Mu, J. Qian, N. Zhang, C. Yang, X. Hou, W. Geng, X. Wang, X. Chou,Nano Energy 68 (2020), 104319.
[10] S. Khan, H. Ali, M. Khalily, S.U.A. Shah, J.U.R. Kazim, H. Ali, C. Tanougast, IEEE Access 8 (2020) 68548–68558.
[11] C.D. Paola, K. Zhao, S. Zhang, G.F. Pedersen, IEEE Access 7 (2019) 73157–73164.
[12] Z. Lü, H. Geng, M. Zhang, X. Hou, Sci. Bull. 53 (2008) 3073–3076.
[13] Z. Qiao, Z. Wang, T. Loh, S. Gao, J. Miao, IEEE Antenn. Wirel. Pr. 18 (2019) 1381–1385.
[14] A.O. Watanabe, B.K. Tehrani, T. Ogawa, P.M. Raj, M.M. Tentzeris, R.R. Tummala, IEEE Trans. Comp. Pack. Man. 10 (2020) 531–533.
[15] C. Huang, J. Li, G. Xie, F. Han, D. Huang, F. Zhang, B. Zhang, G. Zhang, R. Sun, C.P. Wong,Macromol. Mater. Eng. 304 (2019), 1900505.
[16] Z. Liu, B. Song, T. Wang, L. Wang,Appl. Surf. Sci. 512 (2020), 145719.
[17] Z. Wu, N. Li, J. Han, C. Wang, K. Yuan, Q. Zeng, J. Wang, X. Jian, J. Appl. Polym. Sci. 135 (2018) 45976.
[18] J. Dong, C. Yang, Y. Cheng, T. Wu, X. Zhao, Q. Zhang, J. Mater. Chem. C 5 (2017) 2818–2825.
[19] X. Yang, B. Li, D. Li, C. Shao, C. Zhang, J. Eur. Ceram. Soc. 39 (2019) 240–248.
[20] H.Q. Fang, G.Z. Liang, W.S. Zhou, J.Y. Yang, J.L. Wang, China Plast. 19 (2) (2005) 58–61.
[21] W. Li, W. Huang, Y. Kang, Y. Gong, Y. Ying, J. Yu, J. Zheng, L. Qiao, S. Che, Compos. Sci. Technol. 173 (2019) 7–14.
[22] Z. Zhao, G. Zhou, Z. Yang, X. Cao, D. Jia, Y. Zhou, J. Adv. Ceram. (2020), http://dx.doi.org/10.1007/s40145-020-0380-y.
[23] J.R. Oliveira, L.R.V. Kotzebue, D.B. Freitas, A.L.A. Mattos, A.E. da Costa Júnior, S.E. Mazzetto, D. Lomonaco,Compos. Part B-Eng. 194 (2020), 108060.
[24] T. Meireman, L. Daelemans, S. Rijckaert, H. Rahier, W. Van Paepegem, K. De Clerck,Compos. Sci. Technol. 193 (2020), 108126.
[25] X. Huan, K. Shi, J. Yan, S. Lin, Y. Li, X. Jia, X. Yang,Compos. Part B-Eng. 193 (2020), 107987.
[26] P. Samyn, ACS Appl. Mater. Int. (2020), http://dx.doi.org/10.1021/acsami.0c05960.
[27] X. Li, T. Liu, Y. Jiao, J. Dong, F. Gan, X. Zhao, Q. Zhang, Chem. Eng. J. 359 (2019) 641–651.
[28] K. Zhao, L. Cheng, F. Ye, S. Cheng, X. Cui, ACS Appl. Mater. Inter. 11 (2019) 39054–39061.
[29] L. Fumagalli, A. Esfandiar, R. Fabregas, S. Hu, P. Ares, A. Janardanan, Q. Yang, B. Radha, T. Taniguchi, K. Watanabe, G. Gomila, K.S. Novoselov, A.K. Geim, Science 360 (2018) 1339.
[30] S.J. Martin, J.P. Godschalx, M.E. Mills, E.O. Shaffer, P.H. Townsend, Adv. Mater. 12 (2000) 1769–1778.
[31] E.J.G. Santos, E. Kaxiras, ACS Nano 7 (2013) 10741–10746.
[32] Y. Shen, Y.H. Lin, C.W. Nan, Adv. Funct. Mater. 17 (2007) 2405–2410.
[33] X. Yang, B. Li, D. Li, C. Shao, C. Zhang, C. Zou, K. Liu, J. Mater, Sci. Technol. 35 (2019) 2761–2766.
[34] C.H. Wang, L.R.F. Rose, J. Sound Vib. 264 (2003) 851–872.
[35] W. Du, Y. Zhou, Z. Yao, Y. Huang, C. He, L. Zhang, Y. He, L. Zhu, X. Xu,Nanotechnology 30 (2019), 195705.
[36] Z. Man, P. Li, D. Zhou, Y. Wang, X. Liang, R. Zang, P. Li, Y. Zuo, Y.M. Lam, G. Wang, Nano Lett. 20 (2020) 3769–3777.
[37] A. Tang, F. Shen, B. Lan, Y. Ge, J. Li, Y. Duan, Proceedings to the Sixth Symposium on Novel Photoelectronic Detection Technology and Application, Beijing, China, April 1145568, 2020, http://dx.doi.org/10.1117/12.2565218.
[38] W. Guo, C. Mias, N. Farsad, J. Wu, IEEE Trans. Mol. Biol. Multi-Scale Commun. 1 (2015) 18–25.
[39] W. Xia, Y. Han, J. Yang, H. Xie, Hi-Tech Fiber Appl. 28 (2003) 40–43.
[40] X. Hong, Y.Q. Hua, New Chem. Mater. 33 (2005) 16–19.
[41] J. Gu, W. Dong, Y. Tang, Y. Guo, L. Tang, J. Kong, S. Tadakamalla, B. Wang, Z. Guo, J. Mater. Chem. C 5 (2017) 6929–6936.
[42] T. Xiao, J. Kuang, Q. Zheng, S. Xiong, W. Liu, W. Cao,J. Alloys Compd. 831 (2020), 154753.
[43] Y. Park, Y.E. Shin, J. Park, Y. Lee, M.P. Kim, Y.R. Kim, S. Na, S.K. Ghosh, H. Ko, ACS Nano 14 (2020) 7101–7110.
[44] R.M.L. Silva, L. Merces, C.C. Bof Bufon, ACS Appl. Mater. Inter. (2020), http://dx.doi.org/10.1021/acsnano.0c01865.
[45] I. Passchier, D.W. Higinbotham, C.Wd. Jager, B.E. Norum, N.H. Papadakis, N.P. Vodinas, Nucl. Instrum. Methods A 414 (1998) 446–458.
[46] O.S. Jenkins, K.L.C. Hunt, J. Mol. Struct-THEOCHEM 633 (2003) 145–155.
[47] Y. Li, L. Ren, R. Ma, R. Fan, J. Liu, Acta Phys. Sin-Ch. Ed. 59 (2010) 1671–1676.
[48] Q. Wang, D. Sang, H. Jiao, C. Liu, W. Wang, Y. Han, Y. Ma, C. Gao,J. Mol. Struct. 111 (2017), 152903.
[49] R. Wu, G. Zhang, Z. Qiao, R. Chen,Acta Phys. Sin-Ch. Ed. 68 (2019), 128201.
[50] B. Ma, Y. Wang, Y. Chen, Y. Gao, Ceram. Int. 43 (2017) 12209–12212.
[51] Y. Hu, K. Ishikawa,J. Appl. Phys. 59 (2020), 060901.
[52] M.R. Kessler, Polym. Rev. 52 (2012) 229–233.
[53] H.A. Ávila, L.A. Ramajo, M.S. Góes, M.M. Reboredo, M.S. Castro, R. Parra, ACS Appl. Mater. Inter. 5 (2013) 505–510.
[54] K. Krishnadevi, A.N. Grace, M. Alagar, V. Selvaraj, High Perform. Polym. 26 (2013) 89–96.
[55] F. Wang, P. Shi, Aerosp. Mater. Technol. 47 (2017) 10–13.
[56] Y. Liu, J. Dai, X. Liu, J. Luo, S. You, J. Zhu, S. Ma, Z. Jia, J. Electron. Pack. 139 (2017) 31006–31013.
[57] X. Huang, C. Zhi, P. Jiang, D. Golberg, Y. Bando, T. Tanaka, Adv. Funct. Mater. 23 (2013) 1824–1831.
[58] H. Jin, B. Yang, F.L. Jin, S.J. Park, J. Ind. Eng. Chem. 25 (2015) 9–11.
[59] Y.J. Xu, X.H. Shi, J.H. Lu, M. Qi, D.M. Guo, L. Chen, Y.Z. Wang,Compos. Part B-Eng. 184 (2020), 107673.
[60] L. Weng, Y. Zhang, X. Zhang, L. Liu, H. Zhang, Polym. Compos. 39 (4) (2018) 2334–2345.
[61] W. Zhou, J. Cai, J. Appl. Polym. Sci. 124 (2012) 4346–4351.

[62] Z. Lei, J. Ji, Q. Wu, J. Zhang, Y. Wang, X. Jing, Y. Liu,Polymer 178 (2019), 121587.
[63] S. Li, H. Li, Z. Li, H. Zhou, Y. Guo, F. Chen, T. Zhao, Polymer 120 (2017) 217–222.
[64] W. Wu, J. Leng, Z. Wang, H. Qu, J. Gao, Macromol. Res. 24 (2016) 209–217.
[65] G. Hou, B. Cheng, F. Ding, M. Yao, P. Hu, F. Yuan, ACS Appl. Mater. Inter. 7 (2015) 2873–2881.
[66] M. Poorabdollah, M.H. Beheshty, M. Atai, J. Compos. Mater. 50 (2015) 2459–2467.
[67] D.A. Canelas, K.J. Abbey, E. Fentress, J. Appl. Polym. Sci. 86 (2002) 821–843.
[68] T. Hanemann, B. Schumacher, J. Haubelt, Microelectron. Eng. 87 (2010) 15–19.
[69] C. Zhou, G. Liang, A. Gu, RSC Adv. 6 (2016) 6672–6678.
[70] X. Chen, K. Li, S. Zheng, Q. Fang, RSC Adv. 2 (2012) 6504–6508.
[71] K. Sethuraman, T. Lakshmikandhan, M. Alagar, Polym. Compos. 37 (2016) 3433–3441.
[72] X. Li, P. Zhang, J. Dong, F. Gan, X. Zhao, Q. Zhang,Compos. Part B-Eng. 177 (2019), 107401.
[73] S. Köytepe, İ. Küçük, T. Seçkin, H.İ. Adigüzel, Polym.-Plast. Technol. 54 (2015) 1251–1262.
[74] G. Qiu, W. Ma, L. Wu, Polym. Int. 69 (2020) 485–491.
[75] Y. Chen, H. Guo, C. Geng, Y. Wu, G. Dai, C. Teng, J. Mater. Sci.-Mater. El. 30 (2018) 991–1000.
[76] X. Zhao, M. Zhou, Q. Peng, R. Ding, P. Li, Q. Chen, L. Xu, X. He, Adv. Eng. Mater. (2020), http://dx.doi.org/10.1002/adem.202000231.
[77] W. Yao, A. Gu, G. Liang, D. Zhuo, L. Yuan, Polym. Advan. Technol. 23 (2012) 326–335.
[78] Z. Chen, H. Yan, L. Guo, L. Li, P. Yang, B. Liu, Compos. Part A-Appl. S. 121 (2019) 18–27.
[79] J. Hu, A. Gu, G. Liang, D. Zhuo, L. Yuan, Express Polym. Lett. 5 (2011) 555–568.
[80] C. Pan, K. Kou, Q. Jia, Y. Zhang, G. Wu, T. Ji, Compos. Part B-Eng. 111 (2017) 83–90.
[81] Y. Zhou, W. He, N. Wang, D. Xu, X. Chen, M. He, J. Guo, Polym. Eng. Sci. 59 (2019) 1593–1602.
[82] W. Jiang, J. Li, Y. Zhao, P. Luo, D. Li, Aerospace Mater. Technol. 1 (2002) 46–49.
[83] Y. Yuan, Y. Yin, D. Yu, H. Lin, J. Wang, B. Tang, E. Li, J. Mater. Sci.-Mater. El. 28 (2016) 3356–3363.
[84] Z. Jiang, Y. Yuan,Mater. Res. Express 5 (2018), 066306.
[85] X. Zhan, H. Liu, J. Zhang, J. Cheng, X. Lin, Ind. Eng. Chem. Res. 53 (2014) 4254–4262.
[86] M. Zhu, A. Gu, G. Liang, L. Yuan, High Perform. Polym. 25 (2013) 594–608.
[87] I.J. Kim, K. Min, H. Park, S.M. Hong, W.N. Kim, S.H. Kang, C.M. Koo, J. Appl. Polym. Sci. 131 (2014) 40030–40038.
[88] B. Zhang, D. Zhuo, A. Gu, G. Liang, J.T. Hu, L. Yuan, Polym. Eng. Sci. 52 (2012) 259–267.
[89] C. Lin, L. Yuan, A. Gu, F. Chen, G. Liang, Compos. Sci. Technol. 85 (2013) 148–155.
[90] Y. Li, G. Xu, Y. Guo, T. Ma, X. Zhong, Q. Zhang, J. Gu, Compos. Part A-Appl. Sci. Manuf. 107 (2018) 570–578.
[91] C. Xie, Y. Li, Y. Han, Polym. Compos. 37 (2016) 2522–2526.
[92] H. Cao, B. Liu, Y. Ye, Y. Liu, P. Li, Polymers 11 (2019) 950–956.
[93] R. Gao, A. Gu, G. Liang, S. Dai, L. Yuan, J. Appl. Polym. Sci. 12 (2011) 1675–1684.
[94] Z. Sun, P. Huang, A. Gu, G. Liang, L. Yuan, S. Dai, J. Appl. Polym. Sci. 123 (2012) 1576–1583.
[95] Z. Dong, Y. Ni, X. Yang, C. Hu, J. Sun, L. Li, C. Zhou, H. Fan, Compos. Part B-Eng. 153 (2018) 393–397.
[96] L. Fang, J. Zhou, Y. Tao, Y. Wang, X. Chen, X. Chen, J. Hou, J. Sun, Q. Fang, ACS Sustain. Chem. Eng. 7 (2019) 4078–4086.
[97] N. Peelman, P. Ragaert, K. Ragaert, B. De Meulenaer, F. Devlieghere, L. Cardon, J. Appl. Polym. Sci. 132 (2015) 42305–42319.
[98] I. Blanco, F.A. Bottino, Polym. Degrad. Stabil. 121 (2015) 180–186.
[99] L. Zeng, G. Liang, A. Gu, L. Yuan, D. Zhuo, J. Hu, J. Mater. Sci. 47 (2011) 2548–2558.
[100] Z. Zhang, G. Liang, X. Wang, S. Adhikari, J. Pei, High Perform. Polym. 25 (2013) 427–435.
[101] H. Birtane, K. Esmer, S. Madakbas, M.V. Kahraman, J. Macromol. Sci. A 56 (2019) 245–252.
[102] Q. Wei, A. Lazzeri, F. Di Cuia, M.E. Scalari, Macromol. Chem. Phys. 205 (2004) 2089–2096.
[103] Z. Miao, J. Shi, T. Liu, P. Li, Z. Su, G. Wei, Appl. Sci. 9 (2019) 881–892.
[104] C.W. Tsai, K.H. Wu, C.C. Yang, G.P. Wang, React. Funct. Polym. 91 (2015) 11–18.
[105] Y. Tang, L. Yuan, G. Liang, A. Gu, RSC Adv. 4 (2014) 16136–16145.
[106] L. Tang, J. Zhang, Y. Tang, Y. Zhou, Y. Lin, Z. Liu, J. Kong, T. Liu, J. Gu,Compos. Part B-Eng. 186 (2020), 107827.
[107] A. Xing, F. Bao, J. Fu, X. Miao, T. Liu, H. Zhai, X. Cao, Y. Meng, X. Li, Polym. Test. 71 (2018) 38–48.
[108] C. Yuan, J. Wang, K. Jin, S. Diao, J. Sun, J. Tong, Q. Fang, Macromolecules 47 (2014) 6311–6315.
[109] T. Chen, C. Peng, C. Liu, C. Yuan, J. Hong, G. Chen, Y. Xu, L. Dai,Macromol. Mater. Eng. 304 (2018), 1800498.
[110] Z. Liu, J. Zhang, L. Tang, Y. Zhou, Y. Lin, R. Wang, J. Kong, Y. Tang, J. Gu,Compos. Part B-Eng. 178 (2019), 107466.
[111] W.L. Peng, Y. You, P. Xie, M.Z. Rong, M.Q. Zhang, Macromolecules 53 (2020) 584–593.
[112] S.R. Batten, R. Robson, Angew. Chemie Int. Ed. 37 (1998) 1460–1494.
[113] J. Liu, W. Fan, G. Lu, D. Zhou, Z. Wang, J. Yan, Polymers 11 (2019) 862–873.
[114] H.J. Hwang, J.Y. Shieh, C.H. Li, C.S. Wang, J. Appl. Polym. Sci. 103 (2007) 1942–1951.
[115] J. Yang, X. Mao, L. Du, B. Wu, F. Zhang, W. Hu, X. Tang, High Prform. Polym. 30 (2018) 833–839.
[116] Y. Guo, F. Chen, Y. Han, Z. Li, X. Liu, H. Zhou, T. Zhao, J. Polym. Res. 25 (2017) 27–36.
[117] Y. Tu, R. Yu, J. Duan, L. Hu, Iran. Polym. J. 25 (2016) 863–873.
[118] S. Savović, A. Djordjevich, J. Lightwave Technol. 32 (2014) 1290–1294.
[119] P.M. Gore, B. Kandasubramanian, Ind. Eng. Chem. Res. 57 (2018) 16537–16563.
[120] B. Yang, L. Wang, M. Zhang, J. Luo, Z. Lu, X. Ding,Adv. Funct. Mater. 30 (2020), 2000186.
[121] J. Singh, M. Kumar, S. Kumar, S.K. Mohapatra, Polym.-Plast. Technol. 56 (2017) 455–469.
[122] R. Kotek, Polym. Rev. 48 (2008) 221–229.
[123] C. Zhu, B. Wang, J. Meng, S. Deng, X. Fan, T. Peng, W. Zhou, Y. Li, H. Li, C. Zhao,Mater. Res. Express 6 (2019), 095317.
[124] J. Zhou, Y. Li, N. Li, X. Hao, C. Liu, Compos. Sci. Technol. 133 (2016) 173–183.
[125] J. Nasser, J. Lin, K. Steinke, H.A. Sodano, Compos. Sci. Technol. 174 (2019) 125–133.
[126] S. Sharma, A.K. Pathak, V.N. Singh, S. Teotia, S.R. Dhakate, B.P. Singh, Carbon 137 (2018) 104–117.
[127] W. Zhang, P. Yang, Y. Cao, P. Yu, M. Chen, X. Zhou,Constr. Build. Mater. 233 (2020), 117315.
[128] P.S. Shin, J.H. Kim, K.L. DeVries, J.M. Park,Compos. Sci. Technol. 194 (2020), 108166.
[129] M. Ramesh, K. Palanikumar, K.H. Reddy, Compos. Part B-Eng. 48 (2013) 1–9.
[130] B. Qiao, D. Zhou, Z. Dai, W. Zhao, Q. Yang, Y. Xu, X. Li, J. Wu, S. Guo, D. Jiang,Adv. Funct. Mater. 29 (2019), 1808738.
[131] M. Dawood, E. Taylor, S. Rizkalla, Compos. Struct. 92 (2010) 950–963.
[132] J. Parizi, H. Shahverdi, J.J. Roa Rovira, E. Pipelzadeh, M. Martinez, A. Cabot, P. Guardia, ACS Appl. Poly. Mater. (2020), http://dx.doi.org/10.1021/acsapm.0c00295.
[133] H. Masai, N. Iwafuchi, Y. Takahashi, T. Fujiwara, S. Ohara, Y. Kondo, N. Sugimoto, J. Mater. Res. 24 (2009) 288–294.
[134] N.F. Zhernovaya, N.I. Min'ko, V.I. Onishchuk, M.Y. Kochetov, S.A. Borodkin, Glass Ceram. 65 (2008) 109–112.
[135] B. Rath, R. Debnath, A. Paul, P. Velusamy, D. Balamoorthy, Asian J. Civil Eng. 21 (6) (2020) 1051–1066.
[136] J. Ye, J. Fang, L. Zhang, C. Li, Polym. Compos. 39 (2018) 3424–3433.
[137] Q. Chen, T. Linghu, Y. Gao, Z. Wang, Y. Liu, R. Du, G. Zhao, Compos. Sci. Technol. 144 (2017) 202–207.
[138] B. Park, W. Lee, E. Lee, S.H. Min, B.-S. Kim, ACS Appl. Mater. Inter. 7 (2015) 3329–3334.
[139] Y. Han, Y. Xu, Y. Liu, Q. Wang, Z. Zhang, Z. Wang, J. Mater. Chem. A 1 (2013) 10228–10233.
[140] Y. Zhan, Y. Wang, M. Wang, X. Ding, X. Wang,Adv. Mater. Int. 7 (2020), 1901490.
[141] J. Li, J. An, Y. Jiang,J. Chromatogr. A 1620 (2020), 461000.
[142] A. Łapa, M. Cresswell, I. Campbell, P. Jackson, W.H. Goldmann, R. Detsch, A. Parsons, I. Ahmed, A.R. Boccaccini, J. Mater. Chem. B 7 (2019) 6981–6993.
[143] V. Cech, A. Knob, H.A. Hosein, A. Babik, P. Lepcio, F. Ondreas, L.T. Drzal, Compos. Part A-Appl. Sci. Manuf. 58 (2014) 84–89.
[144] K.B. Lim, D.C. Lee, Surf. Interface Anal. 36 (2004) 254–258.
[145] T. Ihara, T. Matsuoka, Y. Iriyama, J. Adhes. Sci. Technol. 10 (1996) 823–832.
[146] H. Li, P. Gu, J. Watson, J. Meng, J. Mater. Sci. 48 (2013) 3075–3087.
[147] B. Wei, H. Cao, S. Song, Mater. Des. 31 (2010) 4244–4250.
[148] V. Tomao, A.M. Siouffi, R. Denoyel, J. Chromatogr. A 829 (1998) 367–376.
[149] K. Cho, G. Wang, R. Raju, G. Rajan, J. Fang, M.H. Stenzel, P. Farrar, B.G. Prusty, ACS Appl. Mater. Int. 11 (2019) 32328–32338.
[150] V.R. Arunprakash, A. Rajadurai, Def. Technol. 13 (2017) 40–46.
[151] N. Karunagaran, A. Rajadurai, J. Mech. Sci. Technol. 30 (2016) 2475–2482.
[152] M. Jing, J. Che, S. Xu, Z. Liu, Q. Fu, Appl. Surf. Sci. 435 (2018) 1046–1056.
[153] S.J. Park, T.J. Kim, J. Appl. Polym. Sci. 80 (2001) 1439–1445.
[154] K. Sever, Y. Seki, I.H. Tavman, G. Erkan, V. Cecen, J. Polym. Res. 30 (2009) 550–558.
[155] K. Sever, M. Sarikanat, Y. Seki, I.H. Tavman, Polym. Compos. 30 (2009) 1251–1257.
[156] N.A. St John, J.R. Brown, Compos. Part A-Appl. Sci. Manuf. 29 (1998) 939–946.
[157] Y. Li, Q. Lin, L. Chen, X. Zhou, Compos. Sci. Technol. 69 (2009) 1919–1924.
[158] H. Zhang, Y. Jiang, Q. Yu, Macromol. React. Eng. 4 (2010) 251–256.
[159] T. Shen, X. Zhou, Q. Lin, Compos. Interface 18 (2012) 701–714.
[160] A. Asadi, M. Miller, R.J. Moon, K. Kalaitzidou, Express Polym. Lett. 10 (2016) 587–597.
[161] P. Nygård, K. Redford, C.G. Gustafson, Compos. Interface 9 (2012) 365–388.
[162] H. He, Z. Duan, W. Liang, Z. Wang, N. Luo,Mater. Res. Express 6 (2019), 125309.
[163] R.H. Zhang, X.T. Shi, Z.Liu L.Tang, J.L. Zhang, Y.Q. Guo, J.W. Gu, Chin. J. Polym. Sci. 38 (2020) 730–739.
[164] W. Zhao, J. Liu, T. Zhao, Modern Radar 38 (2016) 63–66.
[165] L.R. Grace, Compos. Struct. 128 (2015) 305–312.
[166] G. Cui, Y. Cheng, C. Liu, K. Huang, J. Li, P. Wang, X. Duan, K. Chen, K. Liu, Z. Liu, ACS Nano 14 (2020) 5938–5945.

[167] R.L. Wang, F.W. Liu, S.C. Wang, R.L. Wang, M.G. Xia, B. Sun, M.F. Zhu, Mater. Res. Innov. 18 (2014) 859–863.
[168] Q.Y. Luo, P. Wang, N.W. Ding, M. Kuang, H. Peng, L. Xie, Mater. Test. 59 (2017) 708–712.
[169] G. Yu, Y. Hu, D. Lei, J. Funct. Mater. 20 (2014) 20078–20084.
[170] L.X. Zhang, Q. Chang, Z. Sun, J.J. Zhang, J.L. Qi, J.C. Feng, Carbon 154 (2019) 375–383.
[171] M.A. Abd El-baky, M.A. Attia, M.M. Abdelhaleem, M.A. Hassan, J. Compos. Mater. (2020), http://dx.doi.org/10.1177/0021998320928509.
[172] B. Wei, S. Song, H. Cao, Mater. Des. 32 (2011) 4180–4186.
[173] B. Hao, T. Förster, E. Mäder, P.C. Ma, Compos. Part A-Appl. S. 101 (2017) 123–128.
[174] S.O. Lee, S.H. Choi, S.H. Kwon, K.Y. Rhee, S.J. Park, Compos. Part B-Eng. 79 (2015) 47–52.
[175] A. Zhou, Q. Qiu, C.L. Chow, D. Lau, Compos. Part A-Appl. S. (2020), http://dx.doi.org/10.1016/j.compositesa.2020.105802.
[176] V. Manikandan, J.T. Winowlin Jappes, S.M. Suresh Kumar, P. Amuthakkannan, Compos. Part B-Eng. 43 (2012) 812–818.
[177] S. Liu, G. Wu, J. Yu, X. Chen, J. Guo, X. Zhang, P. Wang, X. Yin, Compos. Interface. 26 (2018) 275–290.
[178] B. Wei, H. Cao, S. Song, Compos. Part A-Appl. S 42 (2011) 22–29.
[179] X. Zhang, X. Zhou, H. Ni, X. Rong, Q. Zhang, X. Xiao, H. Huan, J.F. Liu, Z. Wu, ACS Sustain. Chem. Eng. 6 (2018) 2596–2602.
[180] I. Choi, J.G. Kim, D.G. Lee, I.S. Se, Compos.Sci. Technol. 71 (2011) 1632–1638.
[181] S.K. Bhudolia, K.K.C. Kam, S.C. Joshi, J. Ind. Text. 47 (2017) 1887–1907.
[182] B.A. Patterson, H.A. Sodano, ACS Appl. Mater. Inter. 8 (2016) 33963–33971.
[183] L. Zhang, S. Bai, C. Su, Y. Zheng, Y. Qin, C. Xu, Z.L. Wang, Adv. Funct. Mater. 25 (2015) 5794–5798.
[184] S. Fu, B. Yu, L. Duan, H. Bai, F. Chen, K. Wang, H. Deng, Q. Zhang, Q. Fu, Compos. Sci. Technol. 108 (2015) 23–31.
[185] L. Luo, Y. Yuan, Y. Dai, Z. Cheng, X. Wang, X. Liu, Mater. Des. 158 (2018) 127–135.
[186] M. Su, A. Gu, G. Liang, L. Yuan, Appl. Surf. Sci. 257 (2011) 3158–3167.
[187] C. Jia, P. Chen, Q. Wang, J. Wang, X. Xiong, K. Ma, Polym. Compos. 37 (2016) 620–626.
[188] Y. Zhang, Z. Jiang, Y. Huang, Q. Li, Fiber. Polym. 12 (2011) 1014–1020.
[189] A. Nejman, I. Kamińska, M. Cieślak,Plasma Process. Polym. 16 (2019), 1800194.
[190] T.M. Liu, Y.S. Zheng, J. Hu, J. Appl. Polym. Sci. 118 (2010) 2541–2552.
[191] H. Zhang, L. Yuan, G. Liang, A. Gu, Appl. Surf. Sci. 320 (2014) 883–894.
[192] J.S. Lin, Eur. Polym. J. 38 (2002) 79–86.
[193] T. Ai, R. Wang, W. Zhou, Polym. Compos. 28 (2007) 412–416.
[194] H. Pang, R. Bai, Q. Shao, Y. Gao, A. Li, Z. Tang, Appl. Surf. Sci. 359 (2015) 280–287.
[195] X. Zhu, L. Yuan, G. Liang, A. Gu, J. Mater. Chem. A 2 (2014) 11286–11298.
[196] O. Rodríguez-Uicab, F. Avilés, P.I. Gonzalez-Chi, G. Canché-Escamilla, S. Duarte-Aranda, M. Yazdani-Pedram, P. Toro, F. Gamboa, M.A. Mazo, A. Nistal, J. Rubio, Appl. Surf. Sci. 385 (2016) 379–390.
[197] L. Zhou, L. Yuan, Q. Guan, A. Gu, G. Liang, Appl. Surf. Sci. 411 (2017) 34–45.
[198] X. Zhu, L. Yuan, G. Liang, A. Gu, J. Mater. Chem. A 3 (2015) 12515–12529.
[199] R. Sa, Y. Yan, Z. Wei, L. Zhang, W. Wang, M. Tian, ACS Appl. Mater. Inter. 6 (2014) 21730–21738.
[200] L. Tang, J. Dang, M. He, J. Li, J. Kong, Y. Tang, J. Gu, Compos. Sci. Technol. 169 (2019) 120–126.
[201] D. Dai, M. Shi, J. Ind. Text. 47 (2017) 1357–1377.
[202] H. Ning, S. Pillay, N. Lu, S. Zainuddin, Y. Yan, J. Compos. Mater. 53 (2019) 2119–2129.
[203] M. An, H. Xu, Y. Lv, F. Tian, Q. Gu, Z. Eur, Polym. J. 96 (2017) 463–473.
[204] S. Wang, J. Ma, X. Feng, J. Cheng, X. Ma, Y. Zhao, L. Chen, Polym. Compos. 41 (2020) 1614–1623.
[205] X. Jin, W. Wang, C. Xiao, T. Lin, L. Bian, P. Hauser, Compos. Sci. Technol. 128 (2016) 169–175.
[206] L. Shanmugam, X. Feng, J. Yang, Compos. Sci. Technol. 174 (2019) 212–220.
[207] M. Mohammadalipour, M. Masoomi, M. Ahmadi, S. Safi, RSC Adv. 6 (2016) 41793–41799.
[208] J. Claus, R.A.M. Santos, L. Gorbatikh, Y. Swolfs, Compos. Part B-Eng. (2020), http://dx.doi.org/10.1016/j.compositesb.2019.107736.
[209] H. Gu, X. Xu, J. Cai, S. Wei, H. Wei, H. Liu, D.P. Young, Q. Shao, S. Wu, T. Ding, Z. Guo, Chem. Commun. 55 (2019) 10068–10071.
[210] L. Luo, D. Hong, L. Zhang, Z. Chen, X. Liu, Compos. Sci. Technol. 165 (2018) 106–114.
[211] G.M. Wu, Y.T. Shyng, Compos. Part A-Appl. Sci. Manuf. 35 (2004) 1291–1300.
[212] D. Liu, X. Zhou, Y. Zhao, J. Hu, P. Ning, Chem. Res. Appl. 18 (2006) 1171–1174.
[213] J. Gu, T. Bai, J. Dang, J. Feng, Q. Zhang, Fiber. Polym. 14 (2013) 781–785.
[214] Z. Liu, Q. Zeng, P. Chen, Q. Yu, Z. Ding, Vacuum 121 (2015) 152–158.
[215] C.H. Zhang, Y.D. Huang, Y.D. Zhao, Mater. Chem. Phys. 92 (2005) 245–250.
[216] Z. Hu, F. Lu, Y. Liu, L. Zhao, L. Yu, X. Xu, W. Yuan, Q. Zhang, Y. Huang, ACS Appl. Mater. Inter. 10 (2018) 43262–43274.
[217] H. Li, Y. Tang, J. Gu, J. Dang, T. Bai, J. Feng, Polym. Compos. 34 (2013) 2026–2030.
[218] J. Qian, J. Wu, X. Liu, Q. Zhuang, Z. Han, J. Appl. Polym. Sci. 127 (2013) 2990–2995.
[219] P. Zhu, B. Liu, L. Bao, J. Appl. Polym. Sci. 135 (2018) 46852.
[220] L. Yu, F. Lu, X. Huang, Y. Liu, M. Li, H. Pan, L. Wu, Y. Huang, Z. Hu, ACS Appl. Mater. Inter. 11 (2019) 39292–39303.
[221] J. Gu, Y. Li, C. Liang, Y. Tang, L. Tang, Y. Zhang, J. Kong, H. Liu, Z. Guo, J. Mater. Chem. C 6 (2018) 7652–7660.
[222] L. Chen, Y. Du, Y. Huang, F. Wu, H.M. Cheng, B. Fei, J.H. Xin, Compos. Part A-Appl. Sci. Manuf. 88 (2016) 123–130.
[223] Y. Tang, W. Dong, L. Tang, Y. Zhang, J. Kong, J. Gu, Compos. Commun. 8 (2018) 36–41.
[224] L. Tang, J. Zhang, J. Gu, Chin. J. Aeronaut. (2020), http://dx.doi.org/10.1016/j.cja.2020.03.007.
[225] R. Liu, Z. Han, W. Li, X. Li, Q. Zhuang, Polym. Compos. 37 (2016) 1198–1205.
[226] J. Gu, W. Dong, S. Xu, Y. Tang, L. Ye, J. Kong, Compos. Sci. Technol. 144 (2017) 185–192.
[227] D. Hughes, R. Zoughi, IEEE T. Instrum. Meas. 54 (2005) 2398–2401.
[228] X. Xu, B. Zhang, K. Liu, L. Xing, D. Liu, M. Bai, Polym. Test. 72 (2018) 55–62.
[229] Y.F. Gui, W.B. Dou, K. Yin, P.G. Su, Int. J. Infrared Millim. W. 29 (2008) 782–789.
[230] V.N. Egorov, Instrum. Exp. Tech. 50 (2007) 143–175.
[231] Z. Ma, R. Zhao, X. Yang, J. Wei, F. Meng, X. Liu, Mater. Lett. 69 (2012) 30–33.
[232] J. Sheen,Meas. Sci. Technol. 20 (2009), 042001.
[233] J.C.E. Sten, P.K. Koivisto,Meas. Sci. Technol. 20 (2009), 057001.
[234] V.V. Komarov, V.V. Yakovlev, Microw. Opt. Technol. Letters 39 (2003) 443–446.
[235] A. Verma, D.C. Dube, IEEE Trans. Instrum. Meas. 54 (2005) 2120–2123.
[236] C. Chen, F. He, E. Li, J. Yang, Aerospace Mater. Technol. 2 (2013) 99–101.
[237] S. Nam, B. Lee, C. Kwak, J. Lee, IEEE Trans. Microw. Theory (2018) 1228–1237.
[238] R. Rahman, P.C. Taylor, J.A. Scales,Rev. Sci. Instrum. 84 (2013), 083901.
[239] J. Cai, L. Hu, W. Lei, H. Chen, X. Jin, H. Chen, IEEE Trans. Plasma Sci. 43 (2015) 1008–1013.
[240] S. Ge, S. Follonier, A. Knoesen, R.D. Miller, IEEE Microw. Guided Wave Letters 10 (2000) 183–185.
[241] X. Lin, B. Seet, IEEE Trans. Instrum. Meas. 66 (2017) 3100–3102.
[242] N.J. Farcich, J. Salonen, P.M. Asbeck, IEEE Trans. Microw. Theory 56 (2008) 2963–2971.
[243] A. Rotava, R.A.O. Silva, M.H.C. Dias, J.C.A. Santos, IEEE Trans. Microw. Theory 67 (2019) 3506.
[244] M.J. Akhtar, M. Thumm, IEEE Trans. Geosci. Remote 51 (2013) 122–131.
[245] T. Chang, X. Zhang, C. Yang, Z. Sun, H.L. Cui,Meas. Sci. Technol. 28 (2017), 045002.
[246] S.O. Nelson, J. Microwave Power Electromagn. Energy 44 (2010) 98–113.
[247] W. Xu, B.Y. Duan, P. Li, Y. Qiu, IEEE T. Antenn. Propag. 65 (2017) 3175–3183.
[248] C. García, M. Fittipaldi, L.R. Grace, J. Appl. Polym. Sci. 132 (2015), 42691–42670.
[249] A. Martellosio, M. Pasian, L. Perregrini, L. Piffer, R. Riccardi, F. Concaro, P. Besso, IEEE Antenn. Propag. M. 59 (2017) 88–101.
[250] M.E. MacDonald, IEEE Aerospace Electron. Syst. Mag. 34 (2019) 36–43.
[251] Z. Zhu, P. Wang, Appl. Mech. Mater. 40 (2010) 252–256.
[252] Y.L. Chen, Y.W. Jin, Y.L. Chu, X. Zhao, Appl. Mech. Mater. 40 (2011) 252–256.
[253] Z. Qamar, N. Aboserwal, J.L, IEEE Access 8 (2020) 23041–23053.
[254] U. Raveendranath, S. Vandana, S. Sandhya, M. Rakesh, Prog. Electromagn. Res. 154 (2015) 65–78.
[255] B. Zhang, F. Ye, Y. Gao, S. Liu, Q. Liu, D. Ding, Ceram. Int. 42 (2016) 234–241.
[256] P. Pichaimani, S. Krishnan, J.K. Song, A. Muthukaruppan, High Perform. Polym. 30 (2017) 549–560.
[257] J. Zimmermann Ptacek, M. Muggli, S. Wildhack, K. Hintzer, T. Gerdes, M. Willert Porada, R. Moos, J. Appl. Polym. Sci. 135 (2018) 46859.